FEDERAL UNIVERSITY OF SANTA CATARINA
SCHOOL OF TECHNOLOGY
GRADUATE PROGRAM IN CHEMICAL ENGINEERING

Alan Zago de Souza

# CONTRIBUTIONS TO THE NUMERICAL ANALYSIS OF ISOTHERMAL AND INSOLUBLE GAS-LIQUID MICRO-FLOW

Florianópolis/SC
2021

Alan Zago de Souza

# CONTRIBUTIONS TO THE NUMERICAL ANALYSIS OF ISOTHERMAL AND INSOLUBLE GAS-LIQUID MICRO-FLOW

Dissertation for the degree of Master in Chemical Engineering presented to the Graduate Program in Chemical Engineering at Federal University of Santa Catarina.

Advisor: Prof. Dr. Cíntia Soares
Co-advisor: Prof. Dr. Natan Padoin

Florianópolis/SC
2021

Ficha de identificação da obra elaborada pelo autor,
através do Programa de Geração Automática da Biblioteca Universitária da UFSC.

Souza, Alan Zago de
Contributions to the numerical analysis of isothermal and insoluble gas-liquid micro-flow / Alan Zago de Souza ; orientadora, Cíntia Soares, coorientador, Natan Padoin, 2021.
87 p.

Dissertação (mestrado) - Universidade Federal de Santa Catarina, Centro Tecnológico, Programa de Pós-Graduação em Engenharia Química, Florianópolis, 2021.

Inclui referências.

1. Engenharia Química. 2. multiphase flow. 3. micro flow. 4. CFD. 5. numerical analysis. I. Soares, Cíntia. II. Padoin, Natan. III. Universidade Federal de Santa Catarina. Programa de Pós-Graduação em Engenharia Química. IV. Título.

Alan Zago de Souza

**CONTRIBUTIONS TO THE NUMERICAL ANALYSIS OF ISOTHERMAL AND INSOLUBLE GAS-LIQUID MICRO-FLOW**

The present work at the master's level was evaluated and approved by an examining board composed of the following members:

Prof. Dr. Henry França Meier
University of Blumenau

Dr. Karolline Ropelato
ESSS – Engineering Simulation and Scientific Software

We certify that this is the **original and final version** of the conclusion work deemed adequate to obtain the title of Master in Chemical Engineering by the Graduate Program in Chemical Engineering at Federal University of Santa Catarina.

ICP-Edu
Documento assinado digitalmente
Debora de Oliveira
Data: 21/04/2021 19:05:19-0300
CPF: 728.453.929-15
Verifique as assinaturas em https://v.ufsc.br

Prof. Dr. Débora de Oliveira
Coordinator of the Graduate Program in Chemical Engineering

ICP-Edu
Documento assinado digitalmente
Cintia Soares
Data: 21/04/2021 09:41:06-0300
CPF: 020.401.629-09
Verifique as assinaturas em https://v.ufsc.br

Prof. Dr. Cíntia Soares
Advisor

Florianópolis/SC, 2021.

To all who are an inspiration source.

## ACKNOWLEDGEMENTS

I am grateful to my parents, Jairo and Glória, and my brothers and sister, Muriel, Jairo and Isadora, for the continued support and inspiration. I would like to thank all the affection, love and strength to always look forward.

I am grateful to my love, Samara, for the support, companionship and patience. I would like to thank your day by day attention, your affection and love are essential to maintain balance.

I am grateful to my advisors, Prof. Dr. Cíntia Soares and Prof. Dr. Natan Padoin, for the opportunities, guidance and patience. I would like to thank for believing in me and encouraging me to be curious, you are an inspiration source.

I am grateful to members of examining board, Prof. Dr. Henry França Meier and Dr. Karolline Ropelato, for the time spent in evaluating this work. I would like to thank all the valuable contributions, comments and suggestions.

I am grateful to ESSS for the understanding and all support on this work.

I am grateful to my colleagues who directly or indirectly contributed to the achievement on this work.

I am grateful to Federal University of Santa Catarina (UFSC), Graduate Program in Chemical Engineering (PosENQ) and Laboratory of Materials and Scientific Computing (LabMAC) for making this work possible.

“The science of today is the technology of tomorrow.”
(Edward Teller)

## RESUMO

Neste trabalho, um estudo computacional multifásico foi realizado em dispositivos de microcanais. O objetivo foi analisar um escoamento bifásico gás-líquido isotérmico e insolúvel dentro da estrutura de um microcanal retangular usando técnicas de CFD. Uma formulação transiente foi aplicada para capturar a formação do escoamento e as características não permanentes dos padrões avaliados. O método VOF foi utilizado para resolver o escoamento multifásico e uma análise rigorosa foi feita para garantir estabilidade, convergência e confiabilidade para as simulações. A molhabilidade e a tensão superficial foram analisadas em um estudo de caso real, o que permitiu investigar a influência do termo fonte interfacial da equação de conservação de momento no padrão de escoamento e visualizar a transição do padrão de escoamento entre intermitente e estratificado. Este trabalho ajuda a ilustrar alguns aspectos importantes relacionados à simulação multifásica com o método VOF aplicado a microdispositivos e mostra algumas diretrizes para garantir resultados físicos.



**Palavras-chave:** escoamento multifásico, escoamento em microescala, CFD, análise numérica, molhabilidade, tensão superficial.

# RESUMO EXPANDIDO

## Introdução

Na última década, notou-se o esforço de entender e propor mecanismos para os escoamentos em microdispositivos. O sufixo micro indica as dimensões geométricas desses equipamentos. Dispositivos miniaturizados, chamados de microcanais, apresentam um alta razão área/volume e, basicamente, isso cria dois efeitos no escoamento. O primeiro é a mudança das forças dominantes, pois quando o fluido está confinado em uma região do espaço tanto as forças interfaciais como as forças viscosas se sobressaem frente às forças inerciais e gravitacional. O segundo efeito é que a camada limite do escoamento compreende o microcanal, ou seja, o diâmetro do microcanal é a própria espessura da camada limite, e isso intensifica todos os fenômenos de transferência. É importante ressaltar que a teoria da camada limite revolucionou a fluidodinâmica e possibilitou a compreensão de mecanismos de transferência, elucidando que essa camada é responsável por trocas entre o fluido e a superfície. Esses dois efeitos não são notados em escoamentos em macroescalas e ainda possuem muitas questões em aberto em relação a sua fenomenologia. Neste trabalho, foram efetuadas análises que ajudam a compreender os fenômenos envolvidos em dispositivos microfluídicos.

## Objetivos

Nesse contexto, este trabalho tem por objetivo o desenvolvimento de um estudo computacional que possibilite a elucidação dos efeitos encontrados em micro dispositivos com escoamento multifásico gás-líquido isotérmico e insolúvel. Foram avaliados dois estudos utilizando técnicas de fluidodinâmica computacional. O primeiro se refere a um estudo de independência na resolução numérica. Ele é necessário para verificar possíveis variações decorrentes dos parâmetros numéricos e de discretização do modelo computacional. O segundo estudo utiliza os resultados do primeiro para explorar as forças predominantes no escoamento em micro dispositivos. A validação do modelo computacional é efetuada no segundo estudo, no qual os resultados computacionais são confrontados com dados de correlações e experimentais.

## Metodologia

O modelo computacional foi solucionado com a utilização de um solver comercial (ANSYS Fluent 19.2). Foi utilizado o modelo multifásico *Volume of Fluid* (VOF) para resolver o sistema bifásico e um domínio de análise bidimensional foi utilizado para resolver a quantidade de movimento do escoamento. Efeitos de turbulência, transferência de calor e massa e gravidade foram desconsiderados. Todas as simulações são transientes. Dois modelos foram criados, um para o estudo de independência e o outro para o estudo dos efeitos inerentes do escoamento em microescala. O primeiro modelo baseia-se em um domínio reduzido, mas mantendo a representatividade do domínio completo. Foi utilizada uma abordagem com simetria e uma região do domínio foi separada para iniciar com a fase gás. Por fim, velocidade prescrita de líquido foi utilizada na condição de entrada. O segundo modelo utilizou-se das informações obtidas no primeiro estudo. Foi utilizado o domínio completo de um microcanal e a região de mistura das fases pôde ser avaliada. Agora, cada fase possui a sua própria entrada e velocidade prescrita foi utilizada nas duas regiões.

## Resultados e Discussão

O primeiro modelo foi utilizado como caso de testes. Primeiramente, foi feita uma análise com números adimensionais para demonstrar as forças predominantes no escoamento. Constatou-se a grande influência de forças superficiais e viscosas. Três análises foram propostas e utilizadas como critério para independência: análise por resíduo, por passo de tempo e por tamanho de malha computacional. A primeira análise apontou que existem diferenças sutis para os níveis de resíduo analisados, sendo o valor de $1 \cdot 10^{-4}$ o recomendado para garantir a convergência em cada passo de tempo. A segunda análise indicou que valores muito altos para o passo de tempo podem gerar distorções ao longo da simulação, sendo o valor do passo de tempo obtido para um CFL de $2 \cdot 10^{-1}$ suficiente para se obter independência na discretização do tempo. A última análise apresentou resultados sobre o tamanho da malha computacional e indicou a necessidade de maiores cuidados. O valor de $5 \cdot 10^{-6}\ \mathrm{m}$ foi adequado para não favorecer a formação de correntes parasitas e garantir independência em relação à discretização no espaço. O segundo modelo foi utilizado para verificar comportamentos no domínio completo do microcanal. Ainda na etapa de

geração da malha foram apontadas algumas peculiaridades, sendo recomendado alinhar os elementos de malha com as linhas de correntes do escoamento e garantir que não existam elementos com grau de distorção muito elevados no domínio. Três simulações foram efetuadas com três diferentes ângulos de contato. Com isso a molhabilidade foi investigada. Ainda nessa etapa foi feita a validação do modelo computacional. As comparações com correlações e dados experimentais apresentaram boa concordância. Conforme aumentou-se o ângulo de contato, a molhabilidade foi reduzida, e ocorreu a mudança do regime de intermitente para estratificado. Além disso, foi possível capturar uma condição onde o filme líquido não é formado ao redor da cavidade, sendo ela não lubrificada. Com base no comportamento obtido com a variação da molhabilidade, foi possível correlacionar os resultados com o termo fonte da equação de conservação de quantidade de movimento e extrapolar esse mesmo comportamento para outra propriedade, a tensão superficial.

**Considerações Finais**

Este trabalho demonstrou que é possível aplicar técnicas de fluidodinâmica computacional em micro dispositivos para analisar e propor mecanismos de escoamento. Para isso foi elaborada uma metodologia criteriosa de independência para garantir confiabilidade e reprodutibilidade nos resultados. Os resultados gerados a partir dessa metodologia apresentaram boa concordância com dados de correlações e experimentais, mostrando que o modelo é capaz de predizer os fenômenos que ocorrem no funcionamento do micro dispositivo, mesmo tendo forças predominantes diferentes da macro escala. Este estudo contribui para um melhor entendimento das forças superficiais e viscosas presentes em dispositivos microfluídicos.

**Palavras-chave:** escoamento multifásico, escoamento em microescala, CFD, análise numérica, molhabilidade, tensão superficial.

## ABSTRACT

In this work, a multiphase computational study was carried out in microchannel devices. The goal was to analyze a biphasic gas-liquid isothermal and insoluble flow inside a rectangular microchannel structure using CFD techniques. A transient formulation was applied to capture the flow development and the non-permanent flow characteristics. The VOF method was used to resolve the multiphase flow and a rigorous analysis was conducted to ensure stability, convergence and reliability for the simulations. Wettability and surface tension were analyzed on a real study case, allowing us to investigate the influence of the interfacial source term of the momentum conservation equation on the flow pattern and to visualize the flow pattern transition between intermittent and stratified. This work illustrates some critical aspects of the multiphase simulation with the VOF method applied to microdevices and shows some guidelines to ensure physical results.



**Keywords:** multiphase flow, micro-flow, CFD, numerical analysis, wettability, surface tension.

## LIST OF FIGURES

## LIST OF TABLES

## LIST OF ABBREVIATIONS

| | |
|---|---|
| CFD | Computational Fluid Dynamics |
| CFL | Courant-Friedrichs-Lewy |
| CSF | Continuum Surface Force |
| VOF | Volume of Fluid |

## LIST OF SYMBOLS

| | |
|---|---|
| $\alpha_i$ | Volume fraction (-) |
| $\rho_i$ | Density ($kg \cdot m^{-3}$) |
| $p$ | Pressure ($kg \cdot m \cdot s^{-2}$) |
| $\mu_i$ | Dynamic viscosity ($kg \cdot m \cdot s^{-1}$) |
| $\sigma$ | Surface tension ($kg \cdot s^{-2}$) |
| $\kappa$ | Surface curvature ($m^{-1}$) |
| $\theta_w$ | Contact angle ($rad$) |
| $\theta_C$ | Angle between round shape and wall ($rad$) |
| $\delta$ | Liquid film thickness ($m$) |
| $\phi_i$ | General variable () |
| $\boldsymbol{v}$ | Velocity vector ($m \cdot s^{-1}$) |
| $\hat{n}$ | Unit vector normal to the surface (-) |
| $\boldsymbol{g}$ | Gravitational acceleration ($m \cdot s^{-2}$) |
| $D$ | Channel diameter ($m$) |
| $a_i, b$ | Coefficient (-) |
| $C_1$ | Coefficient (-) |
| $J$ | Total superficial velocity ($m \cdot s^{-1}$) |
| $j_i$ | Total volumetric flux ($m^3 \cdot s^{-1}$) |
| $f_{lf}$ | Liquid film function (-) |
| $H$ | Cavity height ($m$) |
| $R_i$ | Residual (-) |
| $u_i$ | Fluid velocity ($m \cdot s^{-1}$) |
| $\Delta P_i$ | Pressure drop ($kPa$) |
| $U_C$ | Cavity velocity ($m \cdot s^{-1}$) |
| $\Delta t_{global}$ | Time-step ($s$) |
| $Bo$ | Bond number (-) |
| $Ca$ | Capillarity number (-) |
| $Re$ | Reynolds number (-) |
| $We$ | Webber number (-) |

**CONTENTS**

# 1 INTRODUCTION

## 1.1 MOTIVATION

The world changed radically after the industrial revolution and the great area of chemical engineering was one of the biggest motors of this process. The focus on increasing chemical production was getting higher to attend to the crescent demand for supplies. Studies about process scale-up began to emerge and the goal of this stage was to create large equipment capable of producing higher quantities. We saw this tendency until the middle of the previous century. Then, scientists started to observe that we should not focus on large-scale structures. Instead, significant development should be directed to small-scale equipment, the so-called microdevices. Benefits like extremely controlled systems, high efficiency, reduced raw material consumption, and reduced waste generation on microchannels become evident (Convery, *et al*., 2019). The suffix micro indicates the geometric scale of this equipment.

The future for chemical processes is to unveil the world of confined spaces and to understand the phenomenology at this scale. To be fair, many scientists are working in this field for almost half-century but in the last two decades, and mainly on the last one, the impact of this field became even more evident and a growing number of people was attracted to study and develop this new technology. Many reasons can be listed for the delay on the eruption of this technology, but the most significant factor was probably the operational difficulty to deal with the microdevices. This barrier started to be broken with the advent of 3D printing, high-speed imaging, precise controllers and high-performance computing, allowing to experiment and investigate microdevices, both numerically and experimentally, with much more detail (Convery, *et al*., 2019).

Microdevices, also called microchannels, microfluidic devices, or miniaturized equipment, show a high surface-to-volume ratio (Gupta, *et al*., 2010). In other words, this means that the fluid is highly confined. Thus, the bulk is reduced and the surface effects start to play a major role. Two main consequences appear when reducing the size scale: a change of the relevant forces and increased mass, heat and momentum transfer rates (Gupta, *et al*., 2010). The former effect occurs due to the modifications of the contributions of each force type on the fluid. In other words, the fluid intrinsic

forces (viscous and interfacial forces) are more relevant when compared to the gravitational and inertial forces, the driving forces in macro-scale. The latter effect is related to the intensification of the transfer phenomena due to the maximization of boundary layer contributions. It is worth to mention that the boundary layer theory made a revolution on fluid dynamics and made it possible the comprehension of the transfer mechanisms, elucidating that this boundary layer is responsible for relevant changes on fluid flow.

As previously commented, numerical and experimental works are being developed in this engineering field, and both are essential to move forward the knowledge about microdevices. While the experimental work investigates the real behavior and is used to validate the numerical works, the numerical approach enables to explore the phenomena in detail. Moreover, a computer-based model allows us to evaluate the effect of varying geometrical and operation conditions with lower costs (time and money). In this sense, computational fluid dynamics techniques contribute significantly to the systematic understanding of microdevices and have been successfully applied in different scenarios. Literature has a vast number of numerical works detailing the dominant forces and the mechanisms of the transfer phenomena correlating different flow properties, like viscosity, density, velocity, and geometrical configurations. But certainly, we are far from getting a full comprehension of the phenomena occurring inside the microdevices, e.g., there is not a flow pattern map available considering all the relevant aspects of the flow in microchannels.

With all the previous comments in mind, this work aims to contribute to the numerical analysis of gas-liquid micro-flow, in the particular condition of isothermal operation and insoluble fluids, considering important numerical aspects that will serve as a reference for the scientist working in this field, as well as the impact of the wettability effect on the flow morphology.

## 1.2 OBJECTIVES

### 1.2.1 General objective

The general objective of this work is to provide guidelines on numerical parameters and to investigate the effect of wettability in isothermal and insoluble gas-liquid micro-flow using computational fluid dynamics (CFD) techniques.

### 1.2.2 Specific objectives

This work focuses on the following specific goals to achieve the general objective:

- investigate the effect of numerical and discretization parameters (residual level, time-step and mesh size) on the performance of CFD simulations of isothermal and insoluble gas-liquid micro-flow;
- propose guidelines for the numerical research on isothermal and insoluble gas-liquid micro-flow, defining optimal conditions to ensure a reliable numerical analysis;
- investigate the effect of the mesh arrangement on the performance of the CFD simulations of isothermal and insoluble gas-liquid flow pattern formation in a T-junction microchannel;
- investigate the effect of wettability on the isothermal and insoluble gas-liquid flow pattern developed in a T-junction microchannel.

## 1.3 STRUCTURE OF THIS DOCUMENT

This document is divided into four chapters. A literature review is provided in chapters 2 and 3, along with the method, the results and the discussion associated with each study performed. Topic conclusions are provided at the end of chapters 2 and 3. All references are listed at the end of this document.

In Chapter 1, the problem is presented and contextualized. A list of objectives to be achieved is presented.

Chapter 2, entitled “Sensibility analysis of CFD techniques applied to isothermal and insoluble gas-liquid micro-flow”, presents the outcome from the first two specific objectives. The numerical independence study made with the reduced case is presented.

Chapter 3, entitled “CFD analysis of the wettability effect on isothermal and insoluble gas-liquid micro-flow”, presents the outcome from the last two specific objectives. The wettability study performed with the complete case is presented.

In Chapter 4, the concluding remarks contemplating all the content previously discussed and suggestions for future works are presented.

# 2. SENSIBILITY ANALYSIS OF CFD TECHNIQUES APPLIED TO ISOTHERMAL AND INSOLUBLE GAS-LIQUID MICRO-FLOW

## 2.1 INTRODUCTION

Different flow types can be seen in nature and industrial equipment. They differ significantly due to the number of phases and the morphology generated, i.e., how a specific phase behaves. When more than one phase is present, the numerical analysis is performed based on different multiphase models. Unlike the thermodynamic definition of a physical phase, a phase in the multiphase approach can be defined as a portion of material that has the same properties and could generate the same responses from interactions of the system (Brennen, 2005). For example, a system with two immiscible liquids is understood as a two-phase configuration from the perspective of a multiphase model.

There are some flow patterns that can categorize all types of multiphase systems. Roughly speaking, we can say that the flows are divided on stratified and intermittent flow (Brennen, 2005). However, it is important to mention that this is a general division and each one contemplates many variations. The field of multiphase numerical simulation requires attention to correctly consider each phenomenon involved (Fletcher, *et al*., 2009) and the first step of any computational study is to verify the flow pattern to apply the recommended multiphase model (Fluent, 2019).

In the last decade, a specific field of computational simulation attracted significant attention: the analysis of the so-called microdevices (Convery, *et al*., 2019). These microfluidic devices are channels in the scale of micrometers that enables to manipulate few microliters per second (Méndez, *et al*., 2017). There are some peculiarities regarding the numerical simulation of microdevices when compared to the well-known macro scale and certainly, this is the driving force of the emphasis on this field. While single-phase flow presents an expected behavior, showing the same aspects of the macro-scale, the multiphase flow does not follow the same trend.

When more than one phase is presented, each fluid has a high surface-to-volume ratio and two main effects appear: a change of the relevant forces and increased mass, heat and momentum transfer rates (Gupta, *et al*., 2010). The former effect occurs due to the modifications of the contributions of each force type on the fluid. In other words, the fluid intrinsic forces (viscous and interfacial forces) are more

relevant when compared to the gravitational and inertial forces, the driving forces in macro-scale. The latter effect is related to the intensification of the transfer phenomena due to the maximization of boundary layer contributions.

When the microdevice has two or more phases, there is a region between the phases called the interface. Physically, this is a well-known thickness that limits the portion of each phase, characterized by an abrupt transition of the physical properties (Faust, *et al*., 2018). On a computational perspective, the resolution of this interface depends on the grid size (Maliska, 2004). The interface region is one of the simulation challenges when dealing with a multiphase model having surface tension and wall adhesion as driving forces (Fletcher, *et al*., 2009). It is essential to ensure good representation of this region to be able to produce reasonable results. Basically, there are two ways to model the surface tension, the continuum surface force (CSF) and continuum surface stress (CSS) (Wörner, 2012) approaches. The first model is related to a localized body force, while the second one is related to the divergence of the surface stress tensor. However, it is important to mention that none of them is capable to correctly predict the balance between the phases in the interfacial region. The unbalance generates the so-called spurious currents, also known as parasite currents (Wörner, 2012), which are unphysical fluid motions when the simulation deals with surface tension as driving force. These artificial currents appear since the discrete domain fails to correctly estimate the surface curvature at the interface (Harvie, *et al*., 2005) and, as a consequence, the pressure term of the momentum conservation equation keeps trying to achieve equilibrium with the source term of interfacial interaction, generating unphysical velocities at the region. However, the remaining terms of the momentum conservation equation can reduce the generation of parasite currents (Harvie, *et al*., 2005). The transient term limits the generation of parasite currents if the interface moves fast relative to the grid due to the surface tension effect. On the other hand, the advective term limits the generation of parasite currents if there is a high local Weber number in a scenario with a well-behaved interface, indicating that the grid is relatively big to the interface motion. Besides that, the spurious currents increase with the reduction of the Capillarity number (Harvie, *et al*., 2005).

It is possible to find works in the literature with new approaches to eliminate the spurious currents and avoid the unphysical velocities on the interface. A height-function surface curvature estimation and consequently balanced-force of CSF model (Popinet, 2009) is capable to correctly calculate the surface curvature in the discrete

domain. It is important to note that this method was only investigated in a stationary fluid, but it is a promising formulation. Another approach is to compute the surface tension term using a specific type of method to convert a continuous field into a discrete one (Chirco, *et al*., 2019), generating satisfactory results with this new approximation. As the parasite currents generate unphysical velocities at the interface, it was also reported that increasing the relative velocity at the interface (Pan, *et al*., 2015), setting a reference frame on the opposite direction of the flow, reduce the generation of these currents. The present work investigates the impact of the spurious currents at the interface and introduces a comprehensive independency study regarding the numerical and discretization parameters, explaining the influence of the time and space discretization, besides the residual level on the resolution of the conservation equations.

## 2.2 METHOD

### 2.2.1 Mathematical model

This study uses a Euler-Euler approach to evaluate the multiphase flow. Conservation equations for each phase are derived to account for the volume fraction, corresponding to the fraction of each phase in the grid cell. To close the equations of multiphase flow it is necessary to provide a constitutive relation through an interfacial model.

The Volume of Fluid (VOF) method was used to resolve the multiphase flow. This technique is capable to model with accuracy the position of the interface in the domain, it is a homogeneous model and allow to resolve only one field for velocity, reducing the computational effort. The surface between the liquid and the gas phases was solved by the conservation equation of volumetric fraction for the secondary phase, in this case the liquid phase, expressed by Eq. 2.1 (Fluent, 2019).

$$\frac{\partial}{\partial t}(\alpha_l \rho_l) + \boldsymbol{\nabla} \cdot (\alpha_l \rho_l \boldsymbol{v}) = 0 \tag{2.1}$$

where $t$ is the time $(s)$, $\alpha$ is the volume fraction $(dimensionless)$, $\rho$ is the density $(kg \cdot m^{-3})$, $v$ is the velocity vector $(m \cdot s^{-1})$ and the subscript $l$ indicates the liquid phase.

The volume fraction of the gas phase is obtained solving the restriction indicated by Eq. 2.2 (Fluent, 2019):

$$\alpha_l + \alpha_g = 0 \tag{2.2}$$

Both the liquid phase and the gas phase share the same momentum conservation equation, according to Eq. 2.3 (Fluent, 2019).

$$\frac{\partial}{\partial t}(\rho \boldsymbol{v}) + \boldsymbol{\nabla} \cdot (\rho \boldsymbol{v}\boldsymbol{v}) = -\nabla p + \boldsymbol{\nabla} \cdot [\mu(\nabla \boldsymbol{v} + \nabla \boldsymbol{v}^{\boldsymbol{T}})] + \rho \boldsymbol{g} + \sigma \kappa \frac{\rho \nabla \alpha_g}{\frac{1}{2}(\rho_l + \rho_g)} \tag{2.3}$$

where $\rho$ is the mixture density $(kg \cdot m^{-3})$, $v$ is the mixture velocity vector $(m \cdot s^{-1})$, $p$ is the pressure field $(kg \cdot m \cdot s^{-2})$, $\mu$ is the mixture dynamic viscosity $(kg \cdot m \cdot s^{-1})$, $g$ is the gravitational acceleration vector $(m \cdot s^{-2})$, $\sigma$ is the surface tension of the liquid-gas pair $(kg \cdot s^{-2})$, $\kappa$ is the surface curvature $(m^{-1})$, $\alpha$ is the volume fraction $(dimensionless)$ and the subscripts $l$ and $g$ indicate the liquid and gas phases. The mixture density and dynamic viscosity were obtained through the mixture law expressed in Eqs. 2.4 and 2.5 (Fluent, 2019).

$$\rho = \alpha_g \rho_g + (1 - \alpha_g)\rho_l \tag{2.4}$$

$$\mu = \alpha_g \mu_g + (1 - \alpha_g)\mu_l \tag{2.5}$$

The surface curvature κ was calculated as the divergent of the unit vector normal to the surface, according to Eq. 2.6 (Fluent, 2019).

$$\kappa = \boldsymbol{\nabla} \cdot \hat{n} \tag{2.6}$$

where the normal vector to the surface and its unit correspondent are shown in Eqs. 2.7 and 2.8 (Fluent, 2019).

$$n = \nabla \alpha_l \tag{2.7}$$

$$\hat{n} = \frac{n}{|n|} \tag{2.8}$$

When the cells are located next to the wall, the unit normal vector considers a specified contact angle, expressed by Eq. 2.9 (Fluent, 2019).

$$\hat{n} = \hat{n}_w \cos\theta_w + \hat{t}_w \sin\theta_w \tag{2.9}$$

where $\hat{n}_w$ and $\hat{t}_w$ are the unit vectors normal and tangential to the wall, respectively, and $\theta_w$ is the specified contact angle. The contact angle varies from 0° to 180°. A hydrophilic wall is represented by a contact angle ranging from 0° to 90°, while a hydrophobic wall is related to a contact angle ranging from 90° to 180°. The contact angle determines the surface curvature close to the wall, influencing the flow behavior at this region.

The energy and species conservation equations were not solved in this problem, since an isothermal condition was adopted and mass transfer/chemical reactions were neglected.

### 2.2.2 Computational procedure

The numerical simulations were based on an experimental study of gas-liquid flow in rectangular microchannels reported in the literature (Choi, *et al*., 2011), focusing on the effect of wettability and pressure drop in different micro-flow configurations.

Figure 2.1 shows the two-dimension computational domain used for the first step of this study. The geometry was thought as a reduced part of the full microdevices, this was necessary to evaluate several numerical convergence issues. Due to the reduced geometry, the computational grid necessary to resolve the domain was reduced too, saving computational time.

The aspect of the reduced geometry retains the characteristics of the full device. The interaction with the wall and the evolution of the interface inside the domain were evaluated. These are two important features worth of tracking for the analysis and the key points for the numerical evaluation tests.

A separate region was created to ensure the same quantity of gas in all the cases. The studies were initialized with a patch of gas phase. A symmetry boundary

condition was used to cut in half the domain, and the microchannel diameter was set as 308.5 $\mu m$. Lastly, the length was chosen (2500 $\mu m$) to make possible to analyze the evolution of the cavity throughout the domain.

Figure 2.1 – Computational domain built for the numerical experiments.

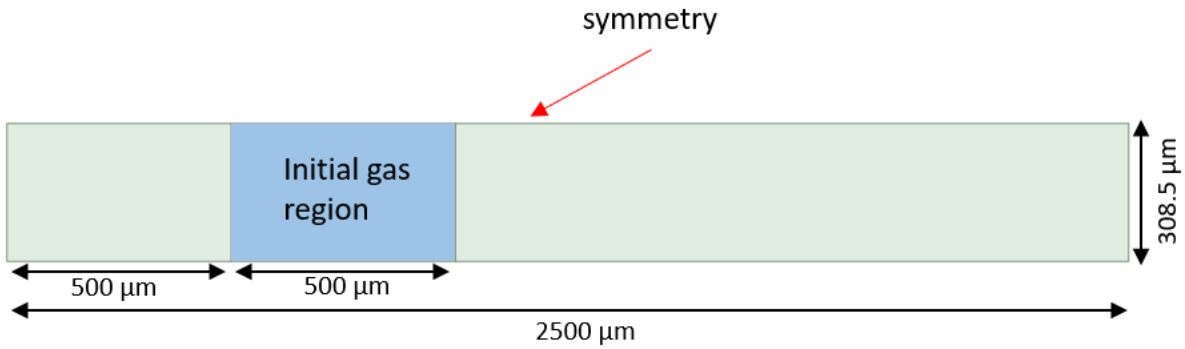


Source: the author (2021).

The grid was composed of quadrilaterals and four mesh densities were adopted, with element sizes within the range of $10\ \mu m$ to $1.25\ \mu m$. Close to the wall (boundary condition located on the opposite region from the symmetry line), a refined mesh layer was considered to adequately capture the gradients.

Figure 2.2 shows a scheme of the boundary conditions adopted for the simulations with the reduced domain. Regarding to the physical setup, a transient and two-dimensional simulation was carried out. The total simulation time was 0.003 s, corresponding to the time interval necessary to observe the evolution of the cavity in the reduced domain. The velocity of the main stream of the full domain ($0.26\ \mathrm{m} \cdot \mathrm{s}^{-1}$) was specified at the inlet, and only the liquid phase enters at this contour. This scenario corresponds to $0.07\ \mathrm{m} \cdot \mathrm{s}^{-1}$ for the gas and $0.19\ \mathrm{m} \cdot \mathrm{s}^{-1}$ for the liquid phase within the full domain. Null gauge pressure was set at the outlet. Moreover, the no-slip boundary condition was adopted at the wall. Water and nitrogen were used as work fluids, with the properties listed in Table 2.1.

Table 2.1 – Properties of the fluids adopted in the numerical experiments.

| Fluid | Density ($\boldsymbol{kg \cdot m^{-3}}$) | Viscosity ($\boldsymbol{kg \cdot m \cdot s^{-1}}$) |
|---|---|---|
| Water | $998.2$ | $1.003 \cdot 10^{-3}$ |
| Nitrogen | $1.138$ | $1.663 \cdot 10^{-5}$ |

Source: the author (2021).

The fluids flow at room temperature and under isothermal conditions. All cases were initialized with the volume fraction for the gas phase equal to 1 over the separate region indicated in Figure 2.1. The surface tension at the gas-liquid interface was set as $0.072\ \mathrm{N} \cdot \mathrm{m}^{-1}$ and the effect of gravity was neglected (considerations about gravity will be further discussed in the results).

Figure 2.2 – Boundary conditions adopted for the numerical experiments in the reduced domain.

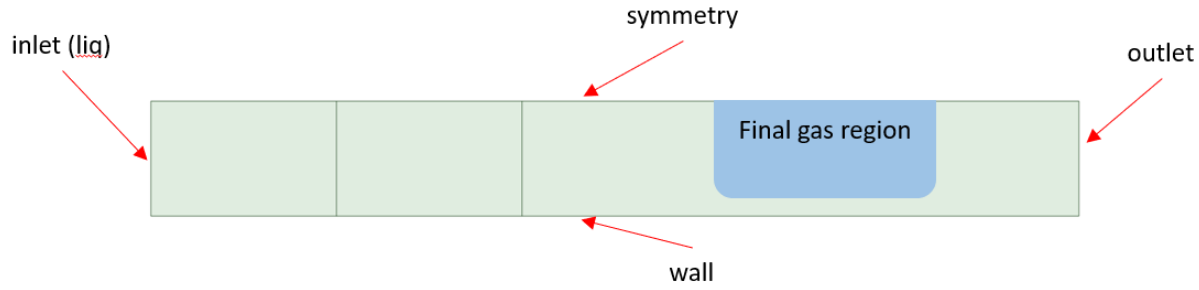


Source: the author (2021).

The simulations were conducted with the commercial software ANSYS® CFD (Fluent®), version 19.2. The discretization of the conservation equations was performed with the finite volume method with the pressure-based solver in a two-dimensional configuration. The velocity-pressure coupling was solved in a segregated form with the SIMPLE algorithm. The gradients were evaluated with the least-squares cell-based method. Besides, the PRESTO! method and the second order upwind scheme were used for the spatial discretization of pressure and momentum, respectively. The geo-reconstruct algorithm was used for the spatial reconstruction of the volumetric fraction. The first order implicit method was used for the time discretization. All sub-relaxation factors were kept at their default values.

All simulations were carried with four processes in parallel, with a processor of 4.2 GHz Intel® Core i7 7700k and 32 GB of RAM memory. The computational time varied from some hours to a few days, depending of the simulation case. A total of 10 cases were investigated with the reduced domain.

Three types of numerical independence studies were evaluated in the reduced geometry: convergence by residuals, by time-step and by grid size. To post-process and compare the results, the pressure, velocity and volume fraction for each case were taken as output variables. The results were extracted in a middle line in a parallel

(length) and perpendicular (height) direction regarding the flow orientation, as shown in Figure 2.3.

Figure 2.3 – Regions for the extraction of the output variables in the numerical experiments carried out in the reduced domain.

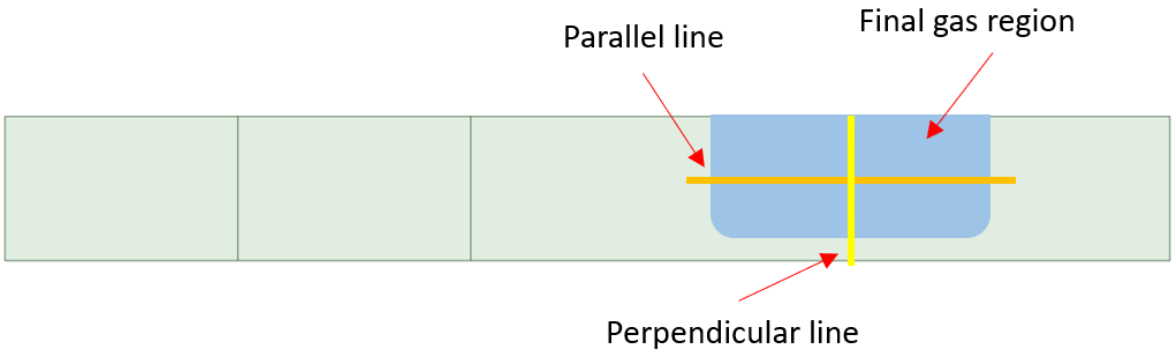


Source: the author (2021).

## 2.3 RESULTS AND DISCUSSION

### 2.3.1 Evaluation of flow characteristic numbers

At the beginning of any simulation study, we need to support the model considered. This is important to justify, for example, the absence of gravity in the computational model. Flow characteristic numbers can indicate the relation between gravitational, interfacial, inertial and viscous forces (Gupta, *et al*., 2010) occurring in micro-flow.

Reynolds number is an important dimensionless group relating the inertial and the viscous forces of the flow (Eq. 2.10). A *Re* below $2.3 \cdot 10^3$ in a smooth circular duct indicates laminar flow; however, *Re* values above that threshold result in a turbulent flow. One should note that when the Reynolds number increase, the inertial force magnitude is increased relative to the viscous force (Gupta, *et al*., 2010).

$$\mathrm{Re} = \frac{inertial\ forces}{viscous\ forces} = \frac{\rho_L u_{LG} D}{\mu_L} \tag{2.10}$$

In the analyzed cases, a *Re* of $1.6 \cdot 10^2$ was observed, indicating that in these simulations the viscous force has is relevant compared to the inertial force and it is not necessary to take into consideration turbulence models.

The Bond (Eötvös) number is another relevant dimensionless group, representing the ratio between gravitational and surface tension forces (Eq. 2.11). This number indicates if gravity or surface tension dominate and helps to decide if all of these effects need to be modeled (Gupta, *et al*., 2010).

$$\mathrm{Bo} = \frac{gravitational\ forces}{surface\ tension\ forces} = \frac{\Delta\rho d^2 g}{\sigma} \tag{2.11}$$

A Bond number below than $1$ indicates a higher influence of surface tension forces over the gravitational forces. In the analyzed cases, we obtained a value of $5 \cdot 10^{-2}$ for this parameter. Some studies suggest a limit to be considered, allowing to neglect the gravitational force. Values below $8.4 \cdot 10^{-1}$ indicates a state of microgravity (Bretherton, 1961) and there is no need to model the gravitational contribution to the flow pattern.

Until this point, we know that our micro-flow simulation has a predominance of viscous and surface tension forces, and this brings us to the next dimensionless group, the Capillary number. This number is built from a composition of the Reynolds and the Webber numbers, according to Eqs. 2.12 and 2.13.

$$\mathrm{We} = \frac{inertial\ forces}{surface\ tension\ forces} = \frac{\rho_L u_{LG}^2 D}{\sigma} \tag{2.12}$$

$$\mathrm{Ca} = \frac{We}{Re} = \frac{\dfrac{inertial\ forces}{surface\ tension\ forces}}{\dfrac{inertial\ forces}{viscous\ forces}} = \frac{viscous\ forces}{surface\ tension\ forces} = \frac{\mu_L u_{LG}}{\sigma} \tag{2.13}$$

A value of *Ca* = $3.62 \cdot 10^{-3}$ was obtained for the analyzed cases, indicating a predominance of the surface tension forces. These two types of force (viscous and surface tension) are the most important ones in micro-flow and helps us to explain what kind of cavity formation mechanism is involved in the microchannel (Oishi, *et al*., 2008).

### 2.3.2 Convergence evaluation by residuals

The finite volume method was used to discretize all the conservation equations, generating a set of algebraic equations. This study will not explain in detail the discretization procedure, but it is possible to find deep description about it elsewhere (Maliska, 2004). A general equation can be written according to Eq. 2.14 (Fluent, 2019).

$$a_P \phi_P = \sum_{nb} a_{nb} \phi_{nb} + b \tag{2.14}$$

where $a_P$ is the center coefficient, $a_{nb}$ are the influence coefficients of the neighboring cells, $\phi_P$ and $\phi_{nb}$ are general variables at the cell $P$ and the neighboring cells, respectively, and $b$ is the contribution of the source term and boundary conditions.

The residue corresponds to the imbalance of the above equation. There are many ways to evaluate the residuals, and this study uses the standard approach of the CFD solver package called globally scaled (Fluent, 2019), defined according to Eqs. 2.15 and 2.16.

$$R_\phi = \frac{\sum_{\text{cells P}} |\sum_{nb} a_{nb} \phi_{nb} + b - a_P \phi_P|}{\sum_{\text{cells P}} |a_P \phi_P|} \tag{2.15}$$

$$R_C = \sum_{\text{cells P}} |\text{rate of mass creation in cell P}| \tag{2.16}$$

where $R_\phi$ and $R_C$ are the residual for a general variable equation and for the continuity equation, respectively.

Judging convergence is always a hard step in the simulation, as there is not a general rule applicable to all cases. It is necessary to evaluate situation per situation to ensure a maximum reliability. In this study we have analyzed three different residual level R: $1 \cdot 10^{-3}$, $1 \cdot 10^{-4}$ and $1 \cdot 10^{-5}$ (note that each residual level represents a reduction of ten time over the previous value).

Figures 2.4 and 2.5 present the pressure and the velocity fields as a function of the channel length, respectively. The liquid fraction is also represented to better

visualize the region of the interface between the liquid and the gas phase. The interface position is invariant for the different residual levels considered. This behavior is also noticed when the pressure profiles are analyzed, i.e., the residual level did not produce significative changes on this variable.

On the other hand, the velocity field shows some variations close to the interface when the residual levels of $1 \cdot 10^{-3}$ and $1 \cdot 10^{-4}$ are considered. However, it remains stable for residuals lower than $1 \cdot 10^{-4}$ (there were no significant differences for the residual levels of $1 \cdot 10^{-4}$ and $1 \cdot 10^{-5}$). The variations in the velocity profile were caused by the low restriction of the residual level and they cannot be assigned to parasite currents (Harvie, *et al*., 2005).

Regarding the cross-section profiles, Figure 2.6 indicates that negligible changes are observed in the velocity and the liquid fraction profiles when the residue level is altered.

Figure 2.4 – Axial pressure and liquid fraction profiles (as a function of the residual level).

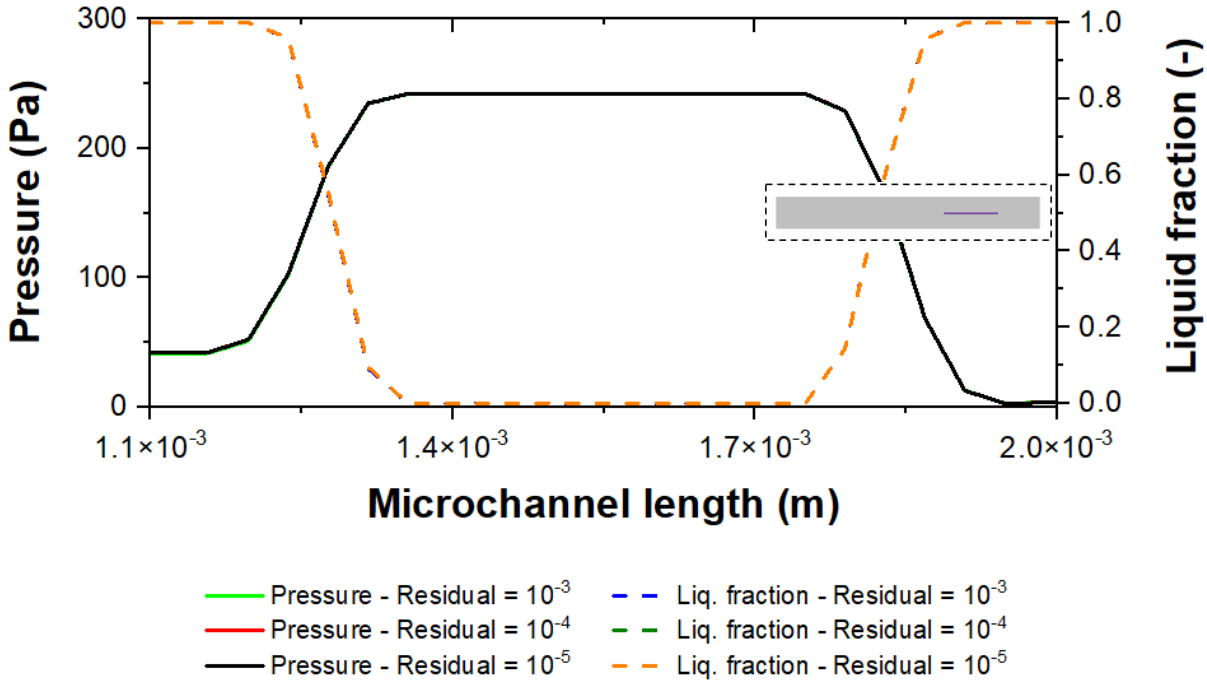


Source: the author (2021).

Figure 2.5 – Axial velocity and liquid fraction profiles (as a function of the residual level).

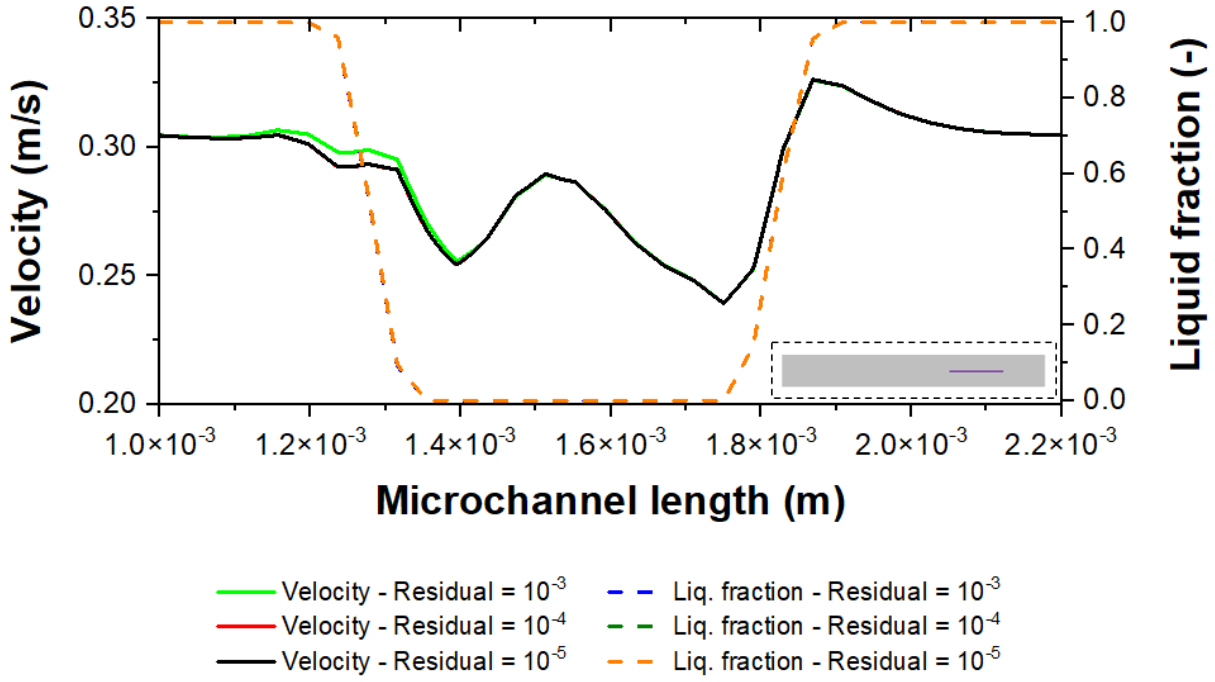


Source: the author (2021).

Figure 2.6 – Cross-section velocity and liquid fraction profiles (as a function of the residual level).

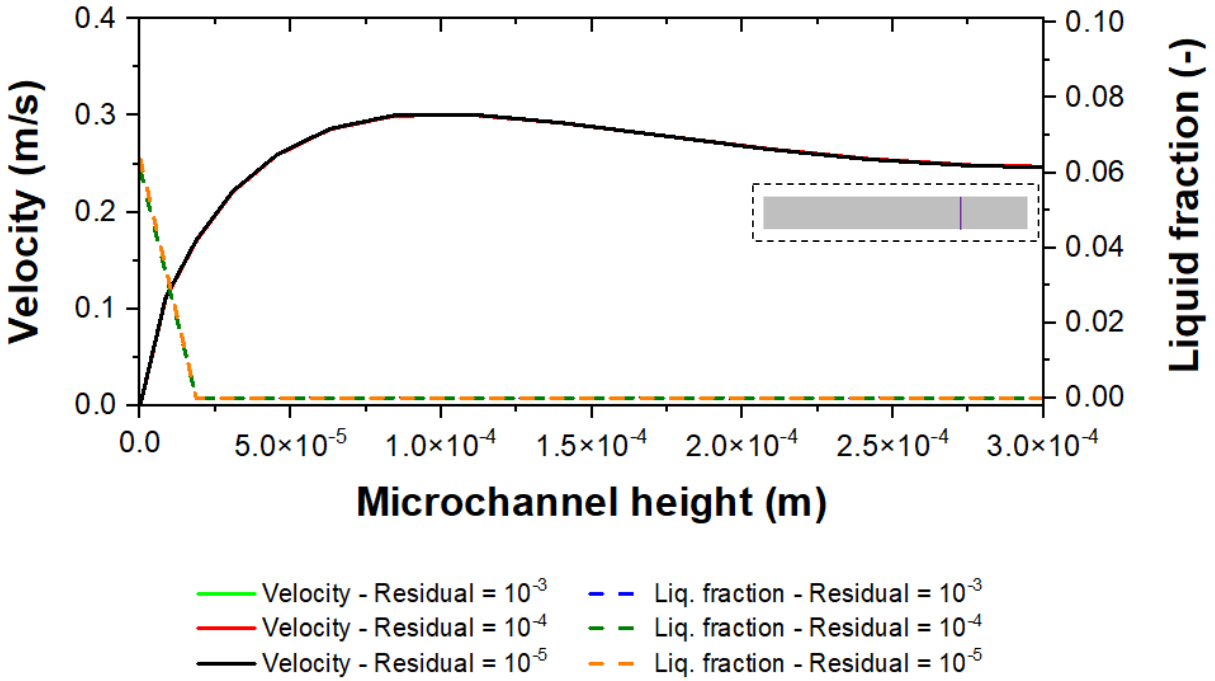


Source: the author (2021).

### 2.3.3 Convergence evaluation by time-step

The time-step used for discretizing the transient term of the conservation equations is crucial to get a smooth and fast convergence on each iteration. Besides that, a relevant point to consider is if the time-step size is reasonable to capture the transient effect of the flow adequately (Gnedin, *et al*., 2018).

Another relevant aspect happens when we are analyzing gas-liquid flow with strong interfacial effects. In this situation it is difficult to predict how the fluid flow will behave and what is the most appropriate value for the time-step size. This scenario requires a robust method to define the time-step, so an adaptive scheme using the Courant-Friedrichs-Lewy ($\mathrm{CFL}$) condition is the preferred choice (LANEY, 1998). This condition is analyzed in all cells to verify the time-step needed to ensure the $\mathrm{CFL}$ number regarding the local velocity and mesh size. In other words, the global time-step will be the lowest value. The time-step size is then computed according to Eq. 2.17 (Fluent, 2019).

$$\Delta \mathrm{t}_{\mathrm{global}} = \frac{\mathrm{CFL}_{\mathrm{global}}}{\max\left(\sum \frac{\text{out going fluxes}}{\text{volume}}\right)} \tag{2.17}$$

where $\mathrm{CFL}_{\mathrm{global}}$ $(\mathrm{dimensionless})$ means the fraction of the cell's information traveling during the time-step, and this value is used for the entire domain.

Three different $\mathrm{CFL}$ numbers, $2 \cdot 10^{0}$, $2 \cdot 10^{-1}$ and $2 \cdot 10^{-2}$, were considered in this study (note that each $\mathrm{CFL}$ number represents a reduction of ten time over the previous value). The time-step size varies to ensure the $\mathrm{CFL}$ condition in all cells. During the simulation the time-step changes to account for the local velocity. The three $\mathrm{CFL}$ numbers generated time-step sizes in the order of $1 \cdot 10^{-6}$ s - $1 \cdot 10^{-8}$ s.

Figures 2.7 and 2.8 present the pressure and the velocity fields along the microchannel's length, respectively. The liquid fraction is also plotted to better visualize the region of the interface between the liquid and the gas phase. The interface does show variations on the position due the $\mathrm{CFL}$ number. The case with $\mathrm{CFL} = 2 \cdot 10^{-0}$ (highest value) displaced the interface and the cavity became more elongated in comparison with the other $\mathrm{CFL}$ numbers tested. Moreover, the pressure and the velocity profiles change when the $\mathrm{CFL}$ number is varied at the levels of of $2 \cdot 10^{-0}$ and

$2 \cdot 10^{-1}$, but stability is reached for $\mathrm{CFL} = 2 \cdot 10^{-1}$ (i.e., there were no significant differences for the $\mathrm{CFL}$ number of $2 \cdot 10^{-1}$ and $2 \cdot 10^{-2}$).

Figure 2.7 – Axial pressure and liquid fraction profiles (as a function of the CFL number).

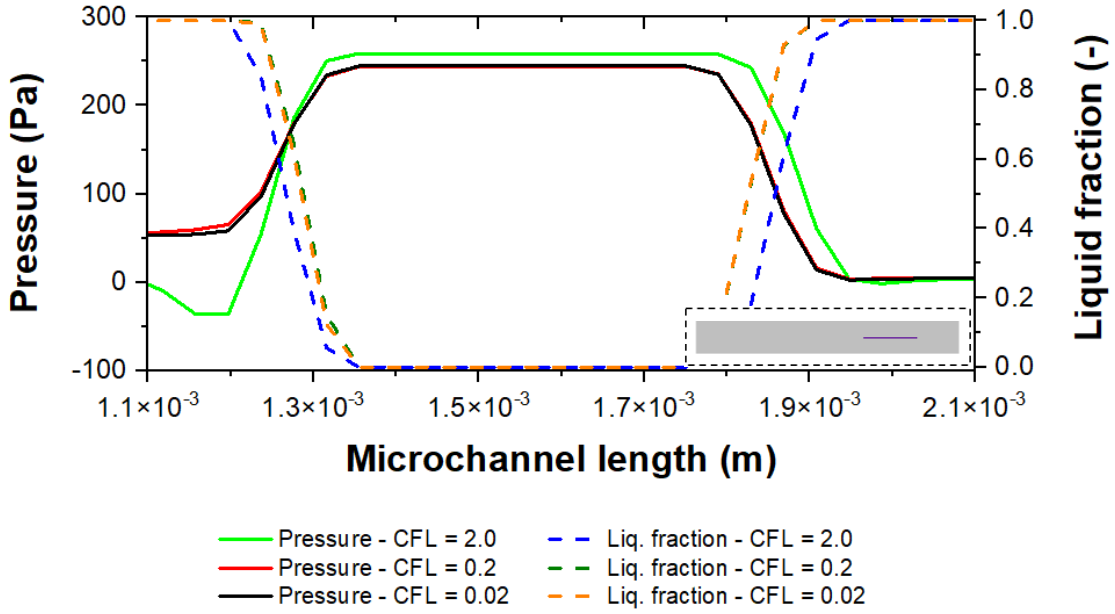


Source: the author (2021).

Figure 2.8 – Axial velocity and liquid fraction profiles (as a function of the CFL number).

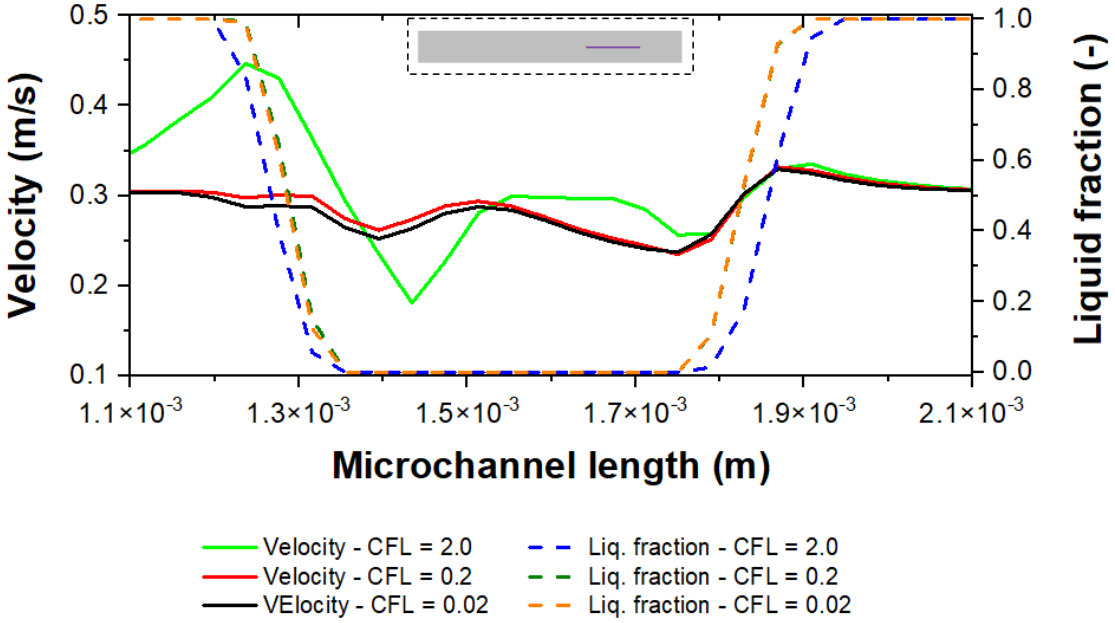


Source: the author (2021).

When the cross-section profiles are analyzed in Figure 2.9, it is possible to verify a similar behavior in comparison with the axial direction analyzed previously, i.e., significant variations only occur in the case with the highest value of $\mathrm{CFL}$. In addition, it is worth to mention that the case with the highest value of $\mathrm{CFL}$ shows a liquid film formation between the cavity and wall, while for the other $\mathrm{CFL}$ numbers this condition is not observed.

Figure 2.9 – Cross-section velocity and liquid fraction profiles (as a function of the CFL number).

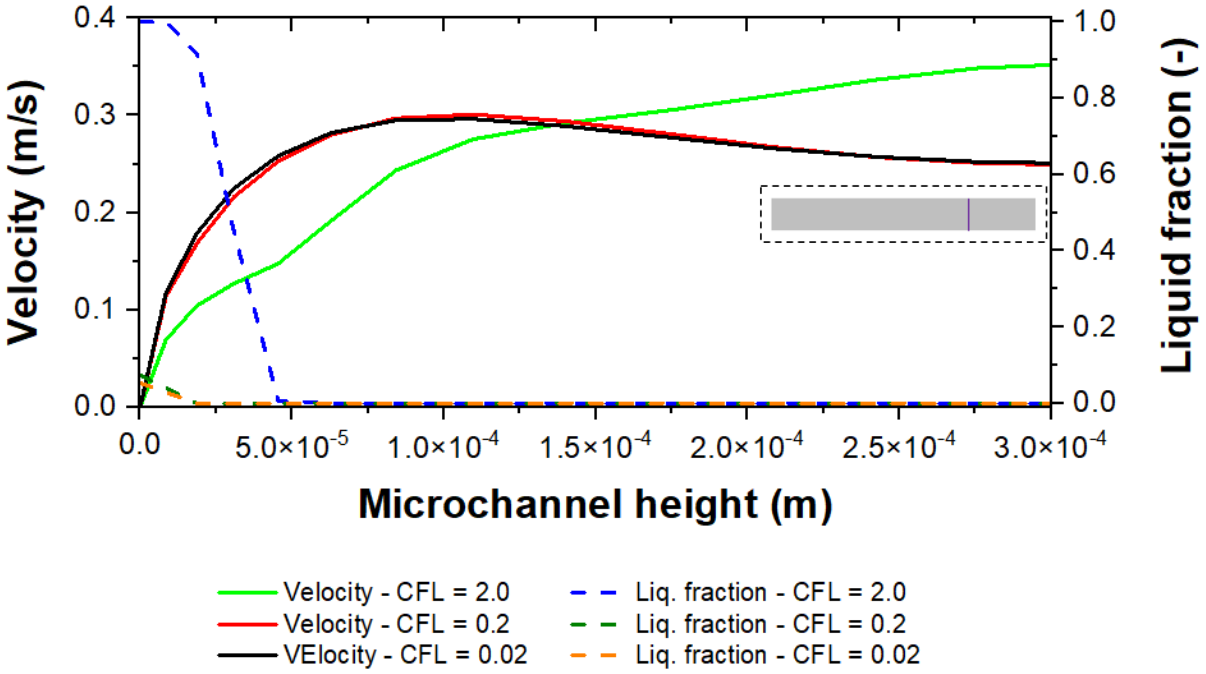


Source: the author (2021).

Even with stabilization for $\mathrm{CFL} = 2 \cdot 10^{-1}$, it is possible to note that the profiles (especially the velocity) do not match perfectly in comparison with the lower $\mathrm{CFL}$ number. These variations can be majorly assigned to the parasite currents. The generation of these currents originates only from the transient (with less impact), advective and diffusive terms of the Navier-Stokes equations (Harvie, *et al.*, 2005).

The plots previously presented showed us that there are significant differences in the liquid fraction fields when the $\mathrm{CFL}$ number is varied, but the stability is achieved when $\mathrm{CFL}$ values equal or less than $2 \cdot 10^{-1}$ were used. Figure 2.10 shows the liquid fraction contour obtained from (a) the case with the highest value of $\mathrm{CFL}$ number $(2 \cdot$

$10^{-0}$) and (b) the cases with $\mathrm{CFL} \leq 2 \cdot 10^{-1}$. The interface resolution was not evaluated here, the goal was to verify the differences regarding the $\mathrm{CFL}$ number.

Figure 2.10 – Fluid pattern obtained from the convergence evaluation by CFL (gas in blue and liquid in red): (a) CFL = 2 and (b) CFL ≤ 0.2.

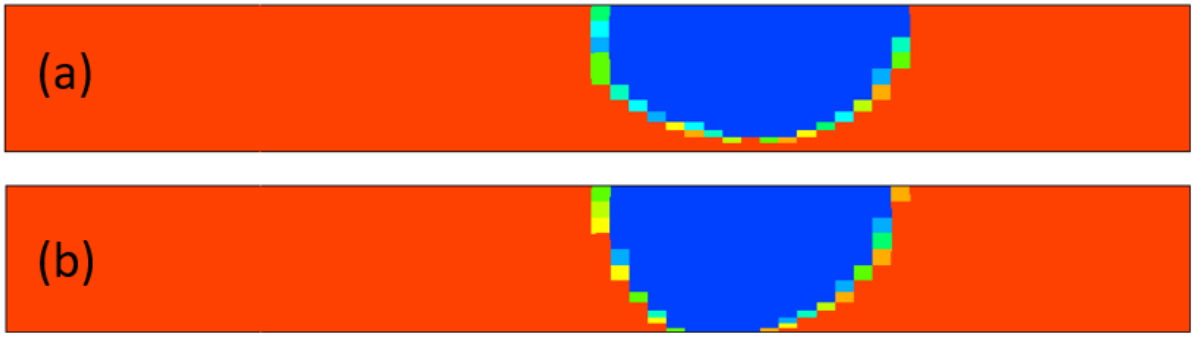


Source: the author (2021).

### 2.3.4 Convergence evaluation by grid size

When we deal with discretized equations, the space is divided in several pieces (grid or mesh) and the analytical solution is only obtained when the grid size tends to zero (infinitely small) (Maliska, 2004). This brings us into an important analysis about the grid independence due the strong relationship between the resolution of results and the grid size.

Four different grid sizes, $1 \cdot 10^{-5}\ \mathrm{m}$, $5 \cdot 10^{-6}\ \mathrm{m}$, $25 \cdot 10^{-7}\ \mathrm{m}$ and $125 \cdot 10^{-8}\ \mathrm{m}$, were evaluated (note that each grid size represents half of the previous value). Quadrilateral elements were used in all simulations.

Figures 2.11 and 2.12 present the pressure and the velocity fields along the microchannel's length, respectively. The liquid fraction is also plotted to better visualize the region of the interface between liquid and gas phase. Essentially, the interface location depends on the mesh resolution, because the information is retained at the center of each cell element of the grid, and indeed the biggest variations occur with the case with larger mesh size $(1 \cdot 10^{-5}\ \mathrm{m})$, while the other mesh sizes maintained the interface location at the same position without significant variations. The pressure profile shows a similar behavior in all cases, and the variations occur due the differences of the interface position.

Figure 2.11 – Axial pressure and liquid fraction profiles (for different mesh refinement).

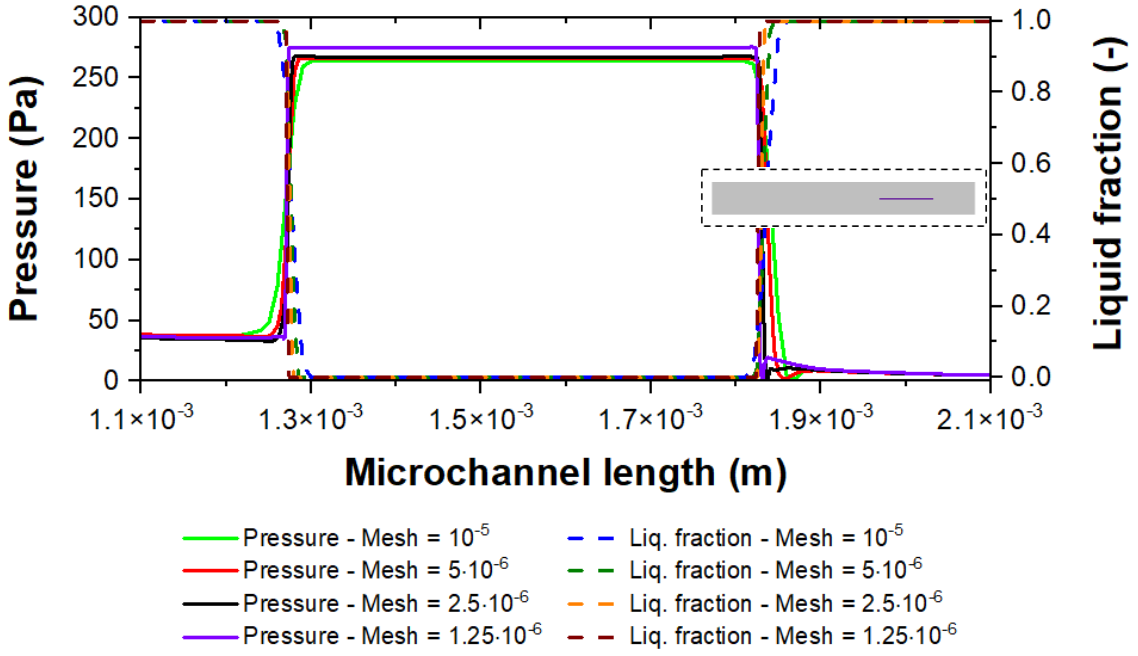


Source: the author (2021).

Figure 2.12 – Axial velocity and liquid fraction profiles (for different mesh refinement).

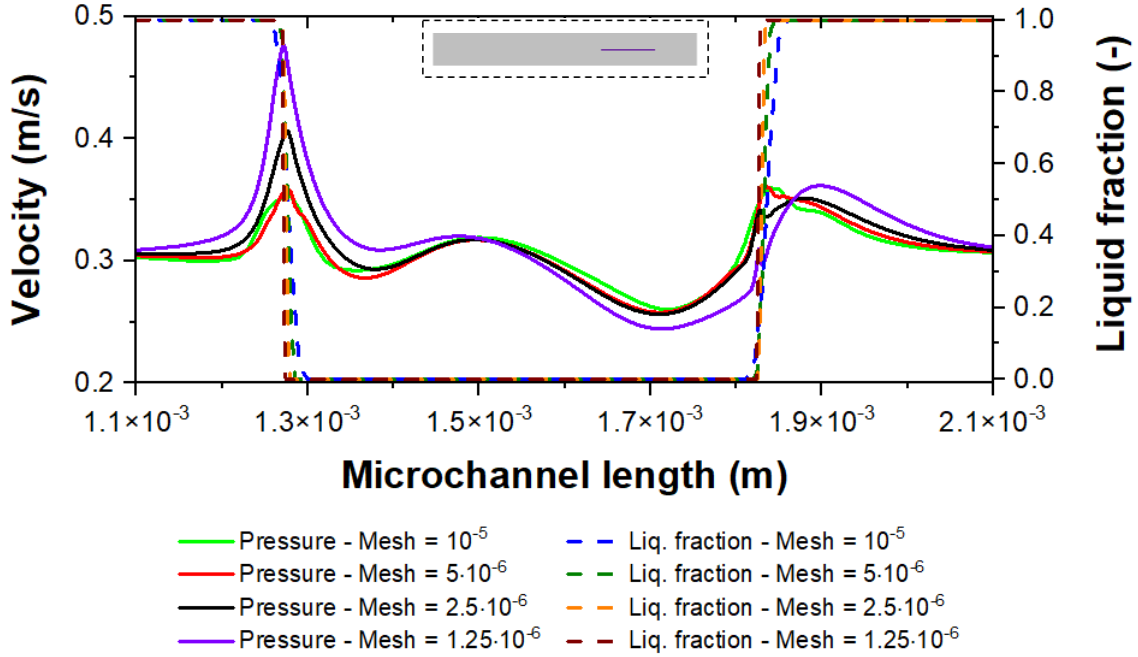


Source: the author (2021).

The velocity profile presents crescent variation as the mesh is reduced, since parasite currents are strongly pronounced as a function of the mesh size. The advective term causes the highest impact on the generation of parasite currents and

its influence is increased with the reduction of the local Weber number (Harvie, *et al*., 2005) (this dimensionless number decreases with decreasing mesh size). It is worth to mention that the parasite currents are been limited by the advective term (Harvie, *et al*., 2005) until the mesh size of $5 \cdot 10^{-6}\,\mathrm{m}$, while lower values for the mesh size increase the peak at the interface region.

Regarding the cross-section profiles, in Figure 2.13 it is possible to verify that the parasite currents are negligible in the perpendicular direction of the flow. The critical situation arises from the equilibrium close to the interface in a parallel direction to the flow, as saw in the previous results. In all cases, a thin liquid film was obtained between the cavity and wall, but the interface location presented the same behavior as the parallel direction, and the case with the larger mesh size $(1 \cdot 10^{-5}\,\mathrm{m})$ showed the more significant variations. Other meshes do not present significant variations of the thin liquid film thickness.

The plots previously presented showed us that the resolution of the interface is closely related to mesh size. Every time the mesh is reduced it will generate differences on the interface resolution. The key point is to determine what resolution the physical model needs.

Figure 2.13 – Cross-section velocity and liquid fraction profiles (for different mesh refinement).

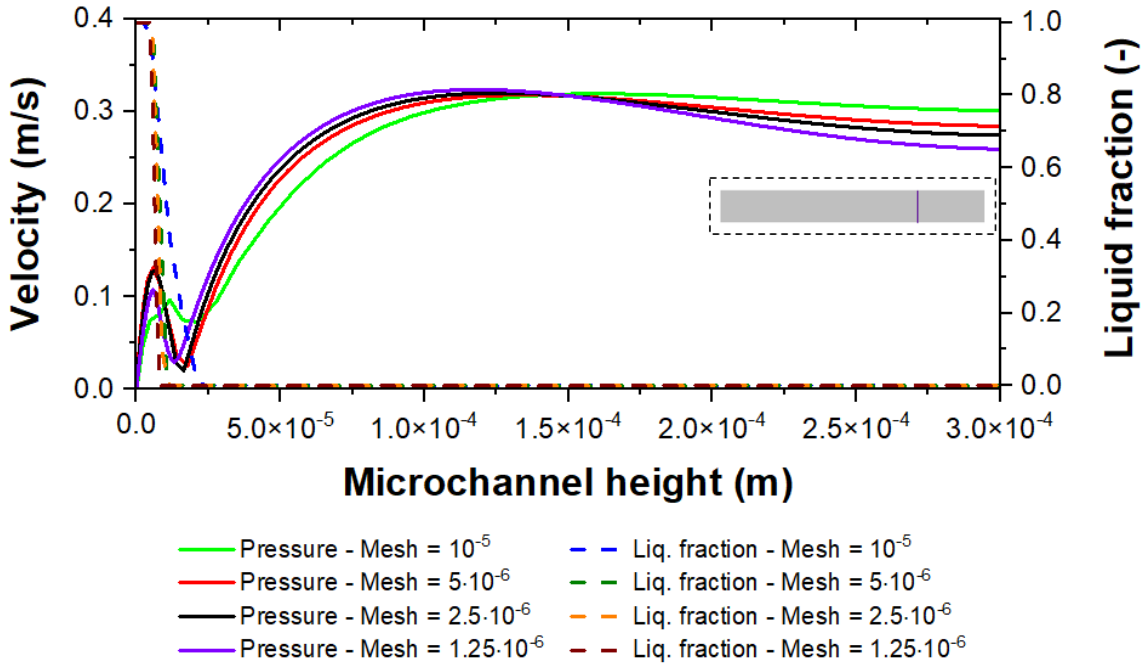


Source: the author (2021).

Figures 2.14 and 2.15 show the liquid fraction contour of two mesh sizes in comparison with a refined one and the difference between them was extracted. It is possible to note a reduction of difference as the mesh size is reduced. For mesh size lower than $5 \cdot 10^{-6}$ m, the variations are not significant regarding the physical model.

Figure 2.14 – Flow pattern obtained from the convergence evaluation by grid size (gas in blue and liquid in red): results from $grid\ size = 25 \cdot 10^{-7} m$, $grid\ size = 1 \cdot 10^{-5} m$ and the difference between them.

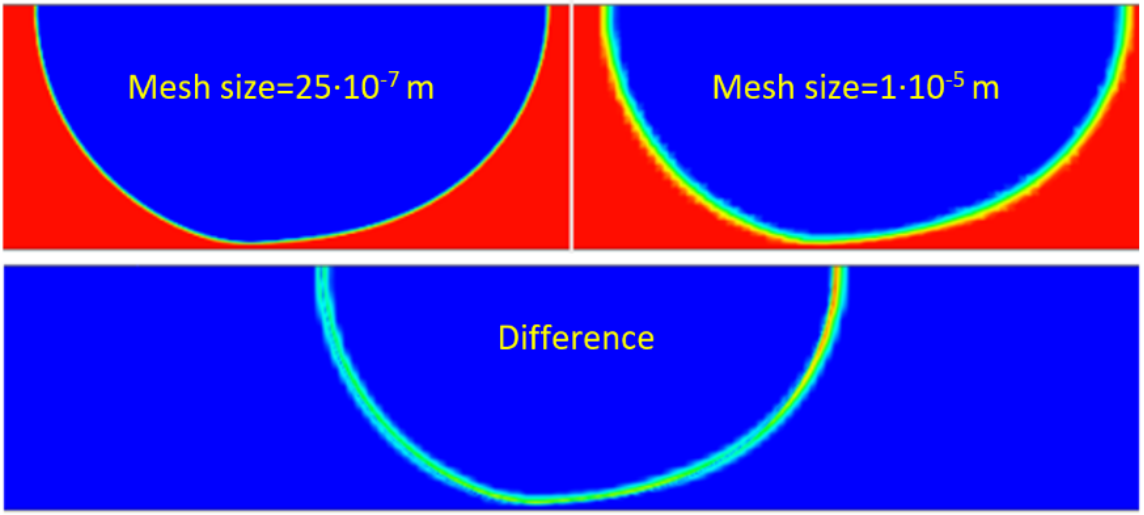


Source: the author (2021).

Figure 2.15 – Flow pattern obtained from the convergence evaluation by grid size (gas in blue and liquid in red): result from $grid\ size = 25 \cdot 10^{-7} m$, $grid\ size = 5 \cdot 10^{-6} m$ and the difference between them.

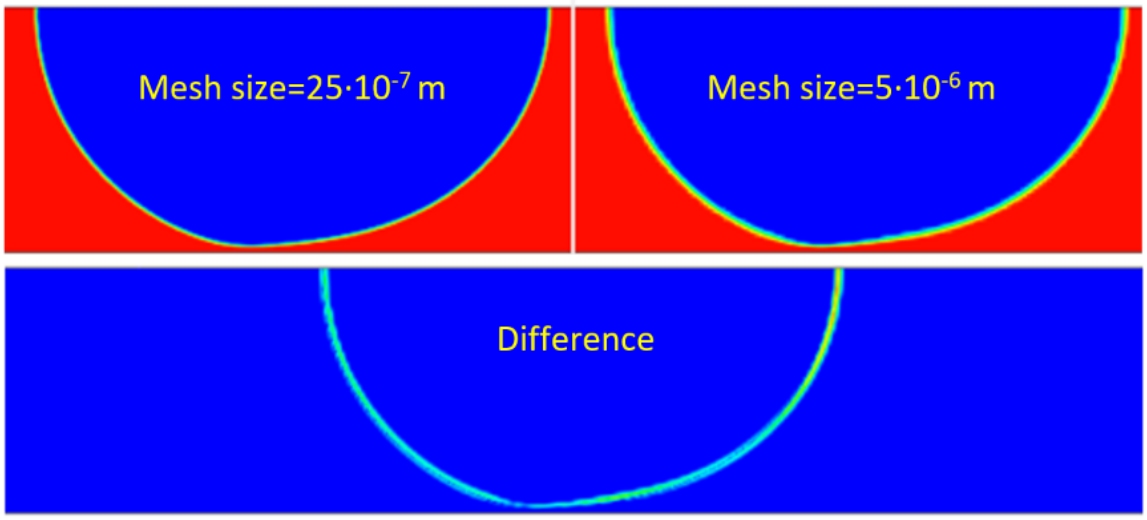


Source: the author (2021).

## 2.4 CONCLUSIONS

Computational studies of microdevices are increasing over time, but it is important to keep in mind some precautions to get reasonable numerical results. This study demonstrates the importance of the resolution and discretization process of a computational multiphase model. A comprehensive analysis was developed to verify the influence of some numerical aspects on the simulation performance. Therefore, it was possible to determine how to reduce interferences and generate independent results.

Firstly, the case study has a reduced Capillary number ($3.62 \cdot 10^{-3}$) which indicates a higher influence of the surface tension forces relative to the viscous forces. This demands a rigorous numerical methodology to fully-resolve the interface in the entire domain and not only close to the wall.

Table 2.2 shows the parameters required to get independent numerical simulation. Regarding the resolution of the momentum and mass conservation equations, it was observed that values of residual above $1 \cdot 10^{-4}$ are insufficient to ensure convergence of the iterative process. Dealing with transient simulation, the truncation errors propagate over the simulation, resulting in unphysical results.

Table 2.2 – Parameters required for independent numerical analysis.

| | |
|---|---|
| Residual | $\mathbf{1 \cdot 10^{-4}}$ |
| CFL number | $2 \cdot 10^{-1}$ |
| Mesh size (m) | $5 \cdot 10^{-6}$ |

Source: the author (2021).

Discretization of time and space were evaluated to determine their influences on the flow behavior. A variable time-step with a fixed CFL was used. Values above CFL = $2 \cdot 10^{-1}$ demonstrate to generate a dependent solution regarding the time, being values equal or less showed numerical independence. A grid analysis proved to be especially important due to the adverse effects of parasite currents. These effects do not invalidate the numerical analysis with the CSF model, used for modeling the effect of surface tension, but it is essential to assess the impacts of parasite currents on the flow in order to verify the reliability of the CFD outcome. This study demonstrated that

it is possible to achieve a compromise solution on the grid refinement to capture the physics while reducing the generation of parasite currents. A grid size of $5 \cdot 10^{-6}\,\mathrm{m}$ was sufficient to ensure independent results regarding the space, representing more than 125 cells across the diameter. Values above the optimum grid size showed dependent solution and values below increased the generation of parasite currents. It is important to note that parasite currents were affected mainly by the grid size.

# 3. CFD ANALYSIS OF THE WETTABILITY EFFECT ON ISOTHERMAL AND INSOLUBLE GAS-LIQUID MICRO-FLOW

## 3.1 INTRODUCTION

The tendency to create miniaturized equipment initiated in the last century due to the observations of the significant benefits of the small scales, like extremely controlled systems, high efficiency, reduced demand of raw material and reduced waste disposal (Gupta, *et al*., 2010). Many researchers are working in the field of micro-flow chemistry for almost half-century but in the last two decades, and mainly in the last one, it became an impact field with a growing number of people studying and developing this technology (Convery, *et al*., 2019). Many reasons can be listed for the delay on the eruption of this technology, but the most significant factor was probably the operational difficulty to deal with the microdevices. This barrier started to be broken with the advent of 3D printing, high-speed imaging, precise controllers and high-performance computing, allowing to experiment and investigate microdevices, both numerically and experimentally, with much more detail (Convery, *et al*., 2019).

Two-phase micro-flow results in a high surface-to-volume ratio and two main effects appear: a change of the relevant forces and the intensification of the mass, heat and momentum transfer phenomena (Gupta, *et al*., 2010). It is important to note that the second effect can also occur in the well-known macro-scale, where the magnitude of the transfer rates can be modulated manipulating the boundary layer, where the gradients are concentrated. However, in micro-flow the bulk effect is significantly minimized, resulting in a higher density of functionality. The differences for the different scales are even more relevant for the first effect. The change of the relevant forces governing the fluid flow can induce unpredictable modification of scenarios even for similar operation conditions.

Basically, the change of the relevant forces is represented by the increase of the magnitude of the interfacial and viscous forces and reduction of the gravitational and inertial contributions, and this is one of the key points to investigate in micro-flow (Fletcher, *et al*., 2009). Previous contributions in the literature have addressed some relevant aspects affecting the interfacial and the viscous forces in micro-flow, i.e., the effect of surface tension (Kovalchuk, *et al*., 2018) and wettability (Lee, *et al*., 2008). Besides the inherent flow characteristics, the geometry arrangement in micro-

structures also plays a major role on the flow pattern. Previous contributions have investigated the effect of the inclination angle between the two inputs channels (Chen, *et al*., 2013) and different relations for the diameter of the two input channels (Nazari, *et al*., 2018), for instance. However, there are some gaps worth of investigation to push forward the fundamental knowledge in this field.

In micro-flow, a common situation is the presence of a cavity or drop forming an intermittent pattern in the two-phase flow. The wettability effect is one of the main reasons to form and keep stable the pattern on that way. Wettability is a surface effect that measures the interaction between the fluid and the solid wall, and consists of the balance between the adhesive force on the wall and the cohesive force of the molecules that constitutes the fluid. The measurement of this quantity is based on the three-phase contact angle, which is the angle between the solid wall and the gas-liquid interface (Gennes, *et al*., 2003).

The contact angle can vary from 0° to 180°. The range of 0° - 90° results in a hydrophilic (or wetting) solid, while the range 90° - 180° leads to a hydrophobic (or non-wetting) solid. In the first scenario the liquid and the solid surface have high affinity and tend to attract each other, but the behavior is the opposite in a hydrophobic surface. The type of contact angle is another detail that needs attention when dealing with the wettability effect, since one can categorize it as static or dynamic (Ralston, *et al*., 2008). The dynamic contact angle is obtained through the movement of the so-called contact line when the three-phase interface is moving over the solid surface, and the magnitude of the fluid velocity is determinant for this measurement. On the other hand, the static contact angle is obtained under equilibrium conditions for the forces involved.

In addition, the solid wettability gives rise to two distinct mechanisms: wetting and dewetting (Ralston, *et al*., 2008). Weeting is the mechanism related to a complete wet surface, dewetting results in a partial wet. Dewetting is highly dependent on the dynamic contact angle and consequently on the characteristic of the fluid flow moving the contact line.

Numerical analysis of wettability is not an unexplored area. Several studies have contributed to better understanding this phenomenon. For example, it is known the effect of the droplet shape on the flow due to the contact force (Rosengarten, *et al*., 2006). The flow behavior was also investigated in a T-junction geometry (Malekzadeh, *et al*., 2015; Arias, *et al*., 2018). However, a comprehensive analysis

should be carried out regarding the dominant forces and their effects on the flow pattern. The present work aims to contribute to the understanding of the wettability effects on gas-liquid micro-flow, analyzing a range of contact angles and describing how this variable impact the flow pattern. In addition, several observations will be discussed regarding the computational model, the cavity formation mechanisms and the relation between the dominant forces at the micro-scale.

## 3.2 METHOD

### 3.2.1 Mathematical model

This study uses a Euler-Euler approach to evaluate the multiphase flow. The conservation equations for each phase are derived to account for the volume fraction, corresponding to the fraction of each phase in the grid cell. Additionally, an interfacial model is accounted to close the equations of the gas-liquid flow.

The Volume of Fluid (VOF) method was used to resolve the multiphase flow. This technique is capable to model with accuracy the position of the interface in the domain, it is a homogeneous model and allow to resolve only one field for velocity, reducing the computational effort. The surface between the liquid and the gas phases was solved by conservation equation of volumetric fraction for the secondary phase, in this case the liquid phase, expressed by Eq. 3.1 (Fluent, 2019).

$$\frac{\partial}{\partial t}(\alpha_l \rho_l) + \boldsymbol{\nabla} \cdot (\alpha_l \rho_l \boldsymbol{v}) = 0 \tag{3.1}$$

where $t$ is the time $(s)$, $\alpha$ is the volume fraction $(dimensionless)$, $\rho$ is the density $(kg \cdot m^{-3})$, $v$ is the velocity vector $(m \cdot s^{-1})$ and the subscript $l$ indicate the liquid phase. The volume fraction of gas phase is obtained solving the restriction indicated by Eq. 3.2 (Fluent, 2019).

$$\alpha_l + \alpha_g = 0 \tag{3.2}$$

Both the liquid phase and the gas phase share the same momentum conservation equation, according to Eq. 3.3 (Fluent, 2019).

$$\frac{\partial}{\partial t}(\rho \boldsymbol{v}) + \boldsymbol{\nabla} \cdot (\rho \boldsymbol{v}\boldsymbol{v}) = -\nabla p + \boldsymbol{\nabla} \cdot [\mu(\nabla \boldsymbol{v} + \nabla \boldsymbol{v}^{\boldsymbol{T}})] + \rho \boldsymbol{g} + \sigma \kappa \frac{\rho \nabla \alpha_g}{\frac{1}{2}(\rho_l + \rho_g)} \quad (3.3)$$

where $\rho$ is the mixture density $(kg \cdot m^{-3})$, $v$ is the mixture velocity vector $(m \cdot s^{-1})$, $p$ is the pressure field $(kg \cdot m \cdot s^{-2})$, $\mu$ is the mixture dynamic viscosity $(kg \cdot m \cdot s^{-1})$, $g$ is the gravitational acceleration vector $(m \cdot s^{-2})$, $\sigma$ is the surface tension of the gas-liquid pair $(kg \cdot s^{-2})$, $\kappa$ is the surface curvature $(m^{-1})$, $\alpha$ is the volume fraction $(dimensionless)$ and the subscripts $l$ and $g$ indicate the liquid and the gas phases. The mixture density and dynamic viscosity were obtained through the mixture law expressed in Eqs. 3.4 and 3.5 (Fluent, 2019).

$$\rho = \alpha_g \rho_g + (1 - \alpha_g)\rho_l \quad (3.4)$$

$$\mu = \alpha_g \mu_g + (1 - \alpha_g)\mu_l \quad (3.5)$$

The surface curvature κ was calculated as the divergent of the unit vector normal to the surface, according to Eq. 3.6 (Fluent, 2019).

$$\kappa = \boldsymbol{\nabla} \cdot \hat{n} \quad (3.6)$$

where the normal vector to the surface and its unit correspondent are shown in Eqs. 3.7 and 3.8 (Fluent, 2019).

$$n = \nabla \alpha_l \quad (3.7)$$

$$\hat{n} = \frac{n}{|n|} \quad (3.8)$$

When the cells are located close to the wall, the unit normal vector considers a specified contact angle, expressed by Eq. 3.9 (Fluent, 2019).

$$\hat{n} = \hat{n}_w \cos\theta_w + \hat{t}_w \sin\theta_w \quad (3.9)$$

where $\hat{n}_w$ and $\hat{t}_w$ are the unit vectors normal and tangential to the wall, respectively, and $\theta_w$ is the specified contact angle. The contact angle varies from 0° to 180°. A hydrophilic wall is represented by a contact angle ranging from 0° to 90°, while a hydrophobic wall is related to a contact angle ranging from 90° to 180°. The contact angle determines the surface curvature close to the wall, influencing the flow behavior at this region.

The energy and species conservation equations were not solved in this problem, since an isothermal condition was adopted and mass transfer/chemical reactions were neglected.

### 3.2.2 Computational procedure

The setup for the full computational domain was carried out based on the analysis of the reduced domain performed in Chapter 2. The three numerical independence studies previously carried out allowed us to get the most reasonable values for the convergence residual level, time-step level and grid size to model the gas-liquid micro-flow occurring at the microdevice considered herein.

Figure 3.1 shown a scheme detailing the geometry and the boundary conditions for the complete domain. This approach follows a previous study made by our research group (Padoin, *et al.*, 2016). The complete domain consists in a 2D representation of the microchannel taken as reference. It is worth to mention that a 3D geometry could be impractical in terms of computational time and memory/processing requirements.

Figure 3.1 – Boundary conditions for the complete domain.

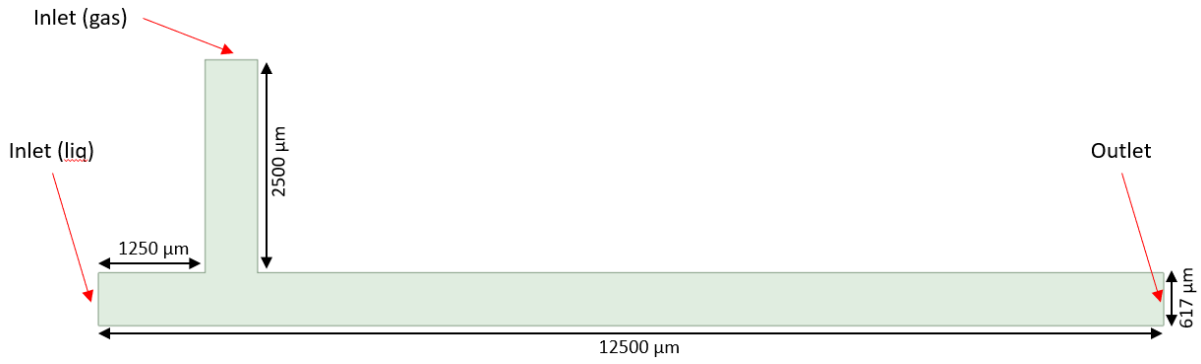


Source: the author (2021).

Each fluid was injected in a different region (inlets). The geometry forms a T-junction mixer, and the fluids get out by an outlet at the end of the main channel. Wall boundary conditions complete the computational model. The microchannel has a diameter of $617\ \mu\mathrm{m}$, the liquid inlet has an extension of $1250\ \mu\mathrm{m}$, and the gas inlet extends up to $2500\ \mu\mathrm{m}$. Additionally, the main channel was evaluated with a length of $12500\ \mu\mathrm{m}$. These dimensions were used due to the good capacity of representation of the evolution of the interfacial liquid-gas region through the domain, retaining the main features of the experimental setup taken as reference.

The grid was composed of quadrilaterals elements with a size of $5\ \mu\mathrm{m}$. Close to the walls, a refined mesh layer was considered to adequately capture the gradients. The wall-clock simulation time depended on each case under study. When simulating the stratified flow pattern, the wall-clock time was around $0.1\ \mathrm{s}$, while for the intermittent situation the wall-clock time was about $0.06\ \mathrm{s}$. An adaptative scheme was used to control the time-step value and the Courant number of $0.2$ was fixed to guide the time-stepping algorithm.

Each case demands a specific time to achieve the statistical stationary state, i.e., a stable operation condition where it is possible to extract quantitative results from the liquid-gas simulation. Velocities of $0.07\ \mathrm{m}\cdot\mathrm{s}^{-1}$ and $0.19\ \mathrm{m}\cdot\mathrm{s}^{-1}$ were set at the gas and liquid inlets, respectively. Null gauge pressure was assumed at the outlet. Moreover, the no-slip boundary condition was adopted at the walls.

All cases were initialized with the volume fraction for the liquid phase equal to 1 over the main channel to facilitate the flow formation and reduce the simulation time to get a stabilize fluid flow. The equations were solved with a residual convergence of $1\cdot 10^{-4}$. All the remaining setup details were the same as the ones adopted and described in Chapter 2.

The computational time was close to six weeks for each simulation case. A total of 6 cases were investigated with the complete domain. Four scenarios of contact angle and surface tension were used to evaluate the wettability effect on the flow pattern. Moreover, two additional tests were conducted to understand some numerical issues (described later in this chapter). To post-process and compare the results, pressure, velocity and volume fraction profiles were extracted for each case. Figure 3.2 shows the locations where the results were analyzed, which consist of lines in parallel (axial) and perpendicular (cross-section) directions regarding the flow

orientation, and two points strategic positioned to follow the evolution of the pressure drop. The perpendicular line and the points to extract the pressure drop are located in the well-developed region of the channel.

Figure 3.2 – Regions of data extraction in the complete domain.

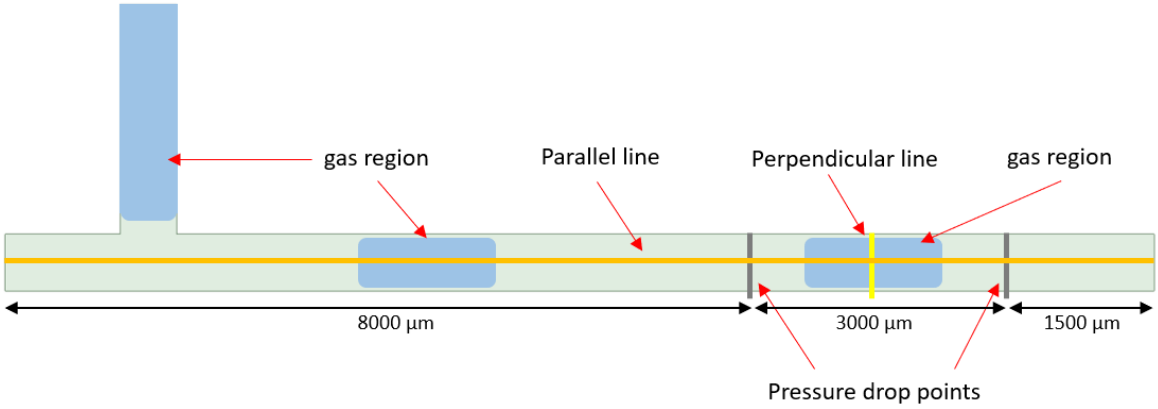


Source: the author (2021).

### 3.2.3 Model evaluation

The cases evaluated in Chapter 2 in the reduced domain were not confronted with experimental data. The idea of these simulations was to understand the numerical behavior, comparing the behavior observed in the different cases. On the other hand, the cases evaluated in the complete domain (this chapter) will be compared with experimental data available in the literature as well with well-known correlations.

Experimental cavity lengths were obtained from the literature under the same operation conditions and retained the main geometrical features (Choi, *et al*., 2011). To evaluate the liquid thin film thickness formed in the intermittent flow, the correlation developed by Han and co-workers was adopted (Han, *et al*., 2010), expressed in Eq. 3.10.

$$\frac{\delta}{D} = \frac{0.670\mathrm{Ca}^{2/3}}{1 + 3.13\mathrm{Ca}^{2/3} + 0.504\mathrm{Ca}^{0.672}\mathrm{Re}^{0.589} - 0.352\mathrm{We}^{0.629}} \tag{3.10}$$

where $\delta$ is the liquid thin film thickness $(\mathrm{m})$, $D$ is the channel diameter $(\mathrm{m})$, $\mathrm{Ca}$ is the Capillarity number $(\mathrm{dimensionless})$, $\mathrm{Re}$ is the Reynolds number $(\mathrm{dimensionless})$ and

$\mathrm{We}$ is the Webber number $(\mathrm{dimensionless})$. The dimensionless numbers are defined specifically for the biphasic flow according to Eqs. 3.11 to 3.13.

$$\mathrm{Ca} = \frac{\mu_L u_G}{\sigma} \tag{3.11}$$

$$\mathrm{Re} = \frac{\rho_L u_G D}{\mu_L} \tag{3.12}$$

$$\mathrm{We} = \frac{\rho_L u_G^2 D}{\sigma} \tag{3.13}$$

where $\mu$ is the dynamic viscosity $(\mathrm{kg \cdot m \cdot s^{-1}})$, $\mathrm{u}$ is the fluid velocity $(\mathrm{m \cdot s^{-1}})$, $\sigma$ is the surface tension of the gas-liquid pair $(\mathrm{kg \cdot s^{-1}})$, $\rho$ is the density $(\mathrm{kg \cdot m^{-3}})$ and the subscripts $\mathrm{L}$ and $\mathrm{G}$ indicate the liquid and the gas phases.

In addition, the cavity pressure drop was computed and confronted with two different correlations. The first one was derived from the experimental study taken as reference (Choi, *et al*., 2011), according to Eqs. 3.14 and 3.15.

$$\Delta P_C = 0.2 U_C^{1.36} \tag{3.14}$$

$$U_C = C_1 J \tag{3.15}$$

where $\Delta P_C$ is the cavity pressure drop $(\mathrm{kPa})$, $U_C$ is the cavity velocity $(\mathrm{m \cdot s^{-1}})$, $C_1$ is a coefficient $(\mathrm{dimensionless})$ and $\mathrm{J}$ is the total superficial velocity $(\mathrm{m \cdot s^{-1}})$.

The second correlation for the cavity pressure drop was derived from an analytical calculation considering a circular channel and a cavity with a cylindrical form (Warnier, *et al*., 2010), expressed in Eq. 3.16.

$$\Delta P_C = \Delta P_L + \Delta P_G \tag{3.16}$$

where $\Delta P_L$ is the frictional pressure drop in the liquid slug and $\Delta P_G$ is the pressure drop caused by the presence of a cavity, according to Eqs. 3.17 and 3.18.

$$\Delta P_L = \frac{64}{Re_T}\frac{L_L}{D}\frac{\rho_L j_T^2}{2} \tag{3.17}$$

$$\Delta P_G = 7.16\frac{\sigma}{D}f_{lf} \tag{3.18}$$

where $Re_T$ is the Reynolds number $(\text{dimensionless})$, $j_T$ is the total volumetric flow rate $(m^3 \cdot s^{-1})$, $L_L$ is the liquid slug length $(m)$ and $f_{lf}$ is a function representing the contribution of the liquid film thickness to the pressure drop $(\text{dimensionless})$. $Re_T$ and $f_{lf}$ (Han, *et al*., 2010) were defined according to Eqs. 3.19 and 3.20.

$$Re_T = \frac{\rho_L j_T D}{\mu_L} \tag{3.19}$$

$$f_{lf} = \frac{(3Ca)^{2/3}}{1 + 3.13Ca^{2/3} + 0.504Ca^{0.672}Re_T^{0.589} - 0.352We^{0.629}} \tag{3.20}$$

The Laplace pressure was also calculated to evaluate the pressure difference between the interior and exterior regions of the cavity. The equation approximates the pressure difference taking into account the angle formed between the round shape of the interface (downstream) close to the wall (Gennes, *et al*., 2003), according to Eq. 3.21.

$$\Delta P = \sigma\frac{2\cos(\theta_C)}{H} \tag{3.21}$$

where $\theta_C$ is the angle formed between the round shape of interface close to the wall, and $H$ is the cavity height $(m)$.

## 3.3 RESULTS AND DISCUSSION

### 3.3.1 Remarks on the mesh generation

The physical case (Choi, *et al*., 2011) has a T-junction region that is fundamental to the formation of the flow pattern. This region presents abrupt variations

of the flow direction, velocity and pressure. The T-junction corner can behave as a singularity point and an intermittent flow can never be formed due to the domain discretization. Therefore, the computational model must be set up taking into account this important observation

It is well-known that micro-flow behaves differently from the macro scale, since the surface forces are dominant in the former case compared to the body forces in the latter one (Ho, *et al*., 1998). Some examples of forces that are important in micro-flow are the surface tension, the viscous force and the wall adhesion (Gupta, *et al*., 2010). Regarding the wall adhesion, the mesh close to the walls needs attention to correctly capture its influence.

Figure 3.3 shows the mesh used for the full geometry analysis. It consisted of $5\times10^5$ quadrilateral elements to correctly discretize the domain. Moreover, it should be highlighted that the grid was built thinking on the flow direction alignment.

Figure 3.3 – Details of the T-junction region for the mesh built for the full geometry and used in all cases: (a) liquid fraction (gas in blue and liquid in red) and (b) mesh.

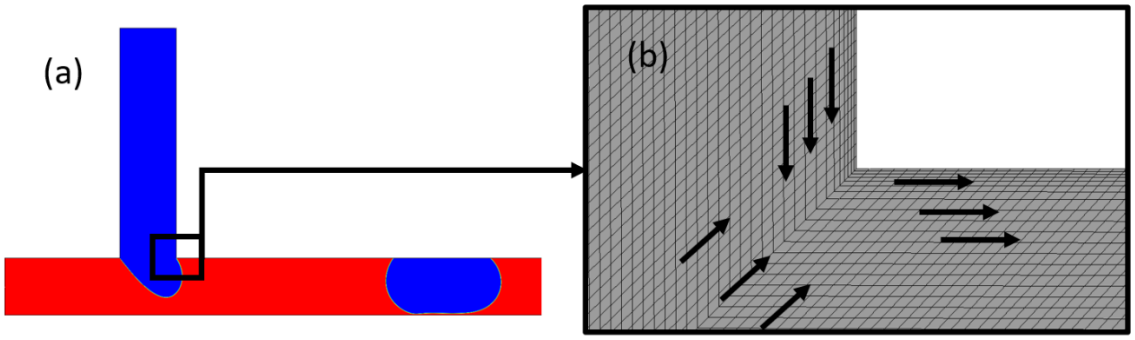


Source: the author (2021).

During the process of grid creation, two issues were observed when analyzing the full geometry. The first one is the numerical diffusion, since the interpolation function used to calculate the flux in each cell element generates a dissipative effect. This dissipative effect could be understood as the truncation errors of the interpolation function used for the advective term of the Navier-Stokes equations and can be reduced if the mesh is aligned with the flow (Maliska, 2004). A numerical diffusion can be observed in Figure 3.4. The oblique flow relative to the mesh avoid the formation of the intermittent flow, while an intermittent flow should indeed be observed given the operation condition tested.

Figure 3.4 – Details of the T-junction region for the mesh built for the full geometry and used to analyze the alignment between the mesh and flow: (a) liquid fraction (gas in blue and liquid in red) and (b) mesh.

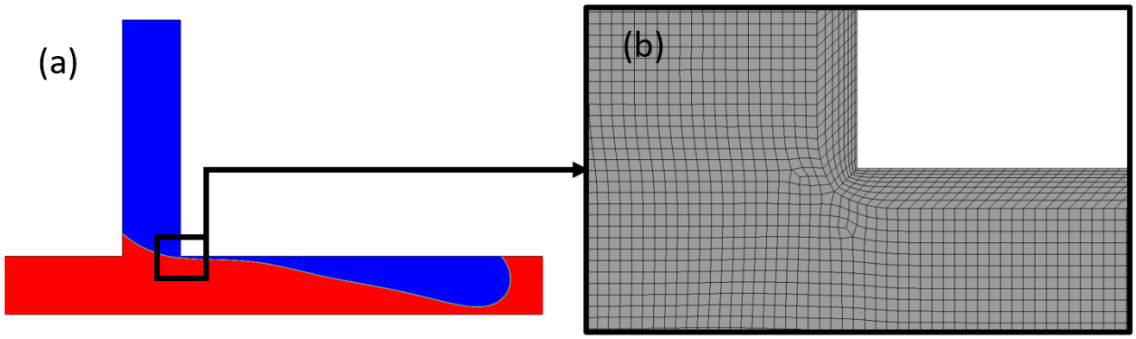


Source: the author (2021).

The second issue is related to the discretization close to the wall. At this boundary it is common to create parallel layers to capture with more accuracy the flow profiles. When micro-flow is considered, a thin liquid film forms between the cavities and the walls (Gupta, *et al*., 2010). This leads to a decrease in mesh size to capture the physics of the system.

A problem could arise from this situation, since a reasonable value for the aspect ratio of the cell elements should be considered. High aspect ratios for the elements lead to inaccurate fluxes. It is important to avoid distorted elements to minimize non-physical behaviors. In the course of this work, we will discuss the cavity formation process, showing that it is related to the interaction between the interface and the wall.

Figure 3.5 presents a distorted behavior due to the high aspect ratio close to the wall. This case generates an intermittent flow but the cavity has a significant difference from the scenario with a reasonable aspect ratio (and from the experimental observation), resulting in a cavity length 23% higher. It is recommended to use a maximum value for the aspect ratio of 5 and to perform a smooth transition between these layers and the interior region (bulk).

Figure 3.5 – Details of the T-junction region for the mesh built for the full geometry and used to analyze the refinement at the wall: (a) liquid fraction (gas in blue and liquid in red) and (b) mesh.

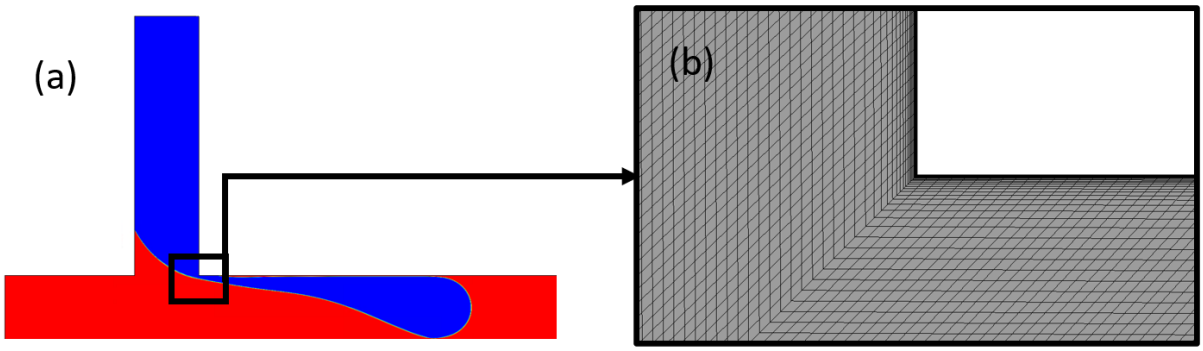


Source: the author (2021).

### 3.3.2 Effect of wettability on the flow pattern

#### *3.3.2.1 Contact angle of 25°*

To understand micro-flow, we must analyze the contribution of two important interfacial forces: the surface tension and adhesive force. The first one is related to the imbalance of cohesive forces of the liquid phase at the surface (or at the interface). It is the amount of energy needed to change the interface area from the minimum energy state, i.e., the smaller the surface tension, the easier will be to redefine the interface area. An effect of the surface tension is the overpressure across the interface. The pressure inside the cavity or bubble (Laplace pressure) with a concave interface will be higher in comparison to the external phase. Adhesion is another important force and consists of the interactions between different molecules. For example, a solid surface could be wet if the liquid molecules have high affinity with the solid surface. This is well-known as wettability and it is measured by a contact angle. The contact angle is a parameter that can vary from 0° to 180°. As shown on Figure 3.6, a contact angle in the range of 0° - 90° results in a hydrophilic (or wetting) wall (Figure 3.6-b), while a contact angle in the range of 90° - 180° result in a hydrophobic (or non-wetting) wall (Figure 3.6-a). In a hydrophilic wall, the liquid and the solid surface have high affinity and tend to attract each other, but the behavior is the opposite when a hydrophobic surface is considered (Gennes, *et al*., 2003).

Figure 3.6 – Illustrations of the wettability effect (contact angle): (a) hydrophobic and (b) hydrophilic wall.

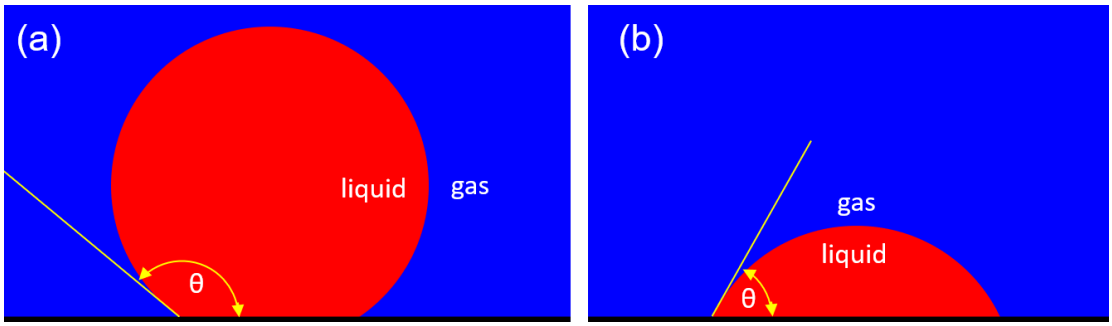


Source: the author (2021).

The cavity formation in micro-flow with low capillarity number has a specific behavior. The driven force formation is not the shear-stress, but the pressure drop upstream to the cavity. Pressure increases due to the reduction of the area for the flow of the main phase, creating a squeezing mechanism that generates a cavity when the interface arrives at the downstream corner (Garstecki, *et al*., 2006). But there are other features that impact the flow pattern and need clarifications, including the wettability and the surface tension (Song, *et al*., 2019).

Figure 3.7 shows the squeezing process obtained from the case with contact angle of 25° (along with the velocity vectors). The low contact angle affects the interaction between the liquid and the wall, so before the cavity separation the velocity vectors shown a tendency of rise on the secondary channel by the liquid. During the process of cavity growing, the area for the gas flow is reduced and a process of interface deformation starts. At this moment, the gas phase is not allowed to flow in the main channel anymore and the pressure-velocity field is reorganized. Note that the liquid in the secondary channel starts to be pushed to the main channel. But an important behavior is noticed here. The region pushing down is far from the wall due the high affinity between the continuous phase and wall and it is attributed to the high surface tension and the tendency to obtain a round interface. At the end of this process, the highly wetted area in the secondary channel and the tendency to form a round interface make the interface to touch the downstream corner of the T-junction, creating a new cavity.

As we know, when we are treating Taylor flow the liquid film around the cavity (or bubble) has an important effect on the transport phenomena (Gupta, *et al*., 2010). But many researchers fail to correctly capture this film due to insufficient mesh

resolution (Fletcher, *et al.*, 2016). Indeed, this study focused to get independent numerical results and the liquid film was considered.

Figure 3.7 – Transient behavior of the cavity formation in the T-junction with contact angle of 25° (gas in blue and liquid in red).

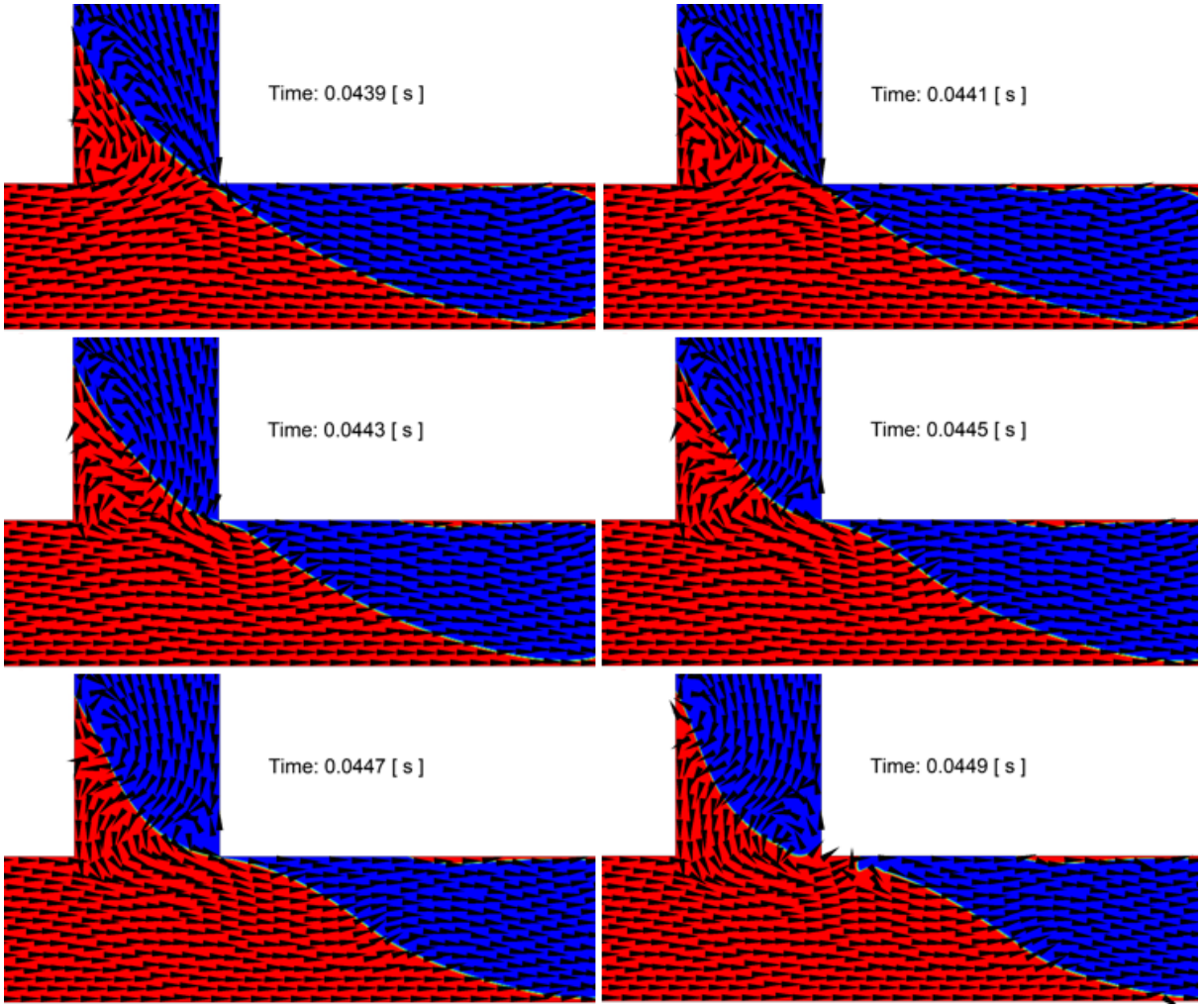


Source: the author (2021).

Figure 3.8 shows the well-developed cavity obtained from the case with contact angle of 25° (along with the velocity vectors). The liquid film (Figure 3.8-c) was captured with a resolution of 5 mesh elements in both regions close to the wall (upper and lower). The velocity vectors on Figure 3.8-a show the presence of parasite currents at the interface region because this pattern has a normal interface parallel to the main flow, and the highest changes are observed in the upstream cavity interface. The velocity field demonstrated to be well-behaved and aligned with the direction of the main flow. Moreover, recirculation patterns are observed when the cavity reference

frame is analyzed (Figure 3.8-b). In fact, Taylor (toroidal) recirculation occurs inside the gas cavities and in the liquid slug, contributing to intensify mass and heat transfer rates.

Figure 3.8 – Cavity well-developed for the contact angle of 25° (gas in blue and liquid in red): (a) lab reference frame, (b) cavity reference frame and (c) liquid film.

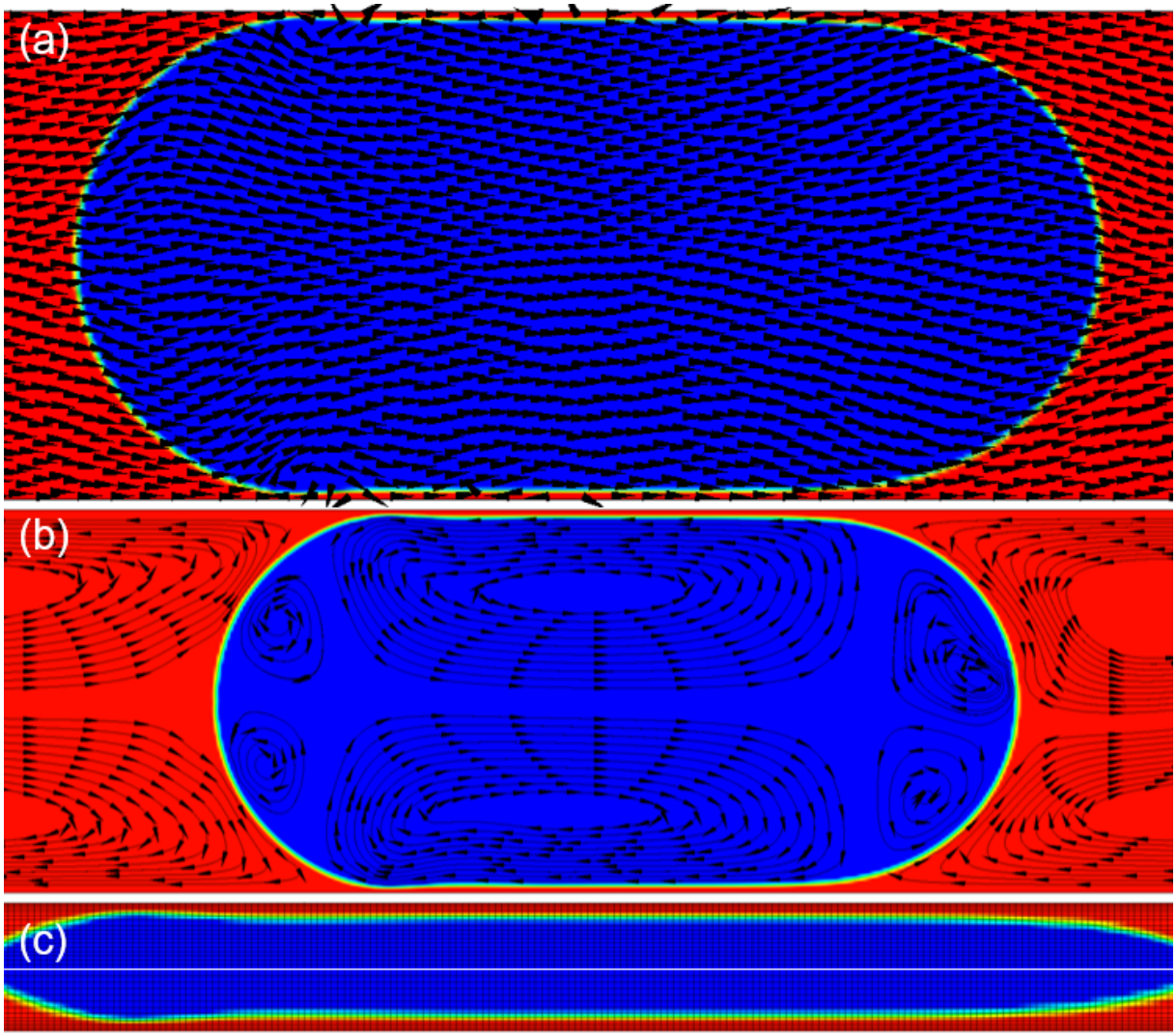


Source: the author (2021).

Figure 3.9 presents the velocity profile at the cross-section of a cavity (located at half of the cavity length). The liquid fraction is also plotted to better visualize the region of the interface between liquid and the gas phase. The behavior of the velocity follows a parabolic profile, with a peak at the middle of the microchannel. Both fluids tend to flow by the middle of the microchannel, but the surface tension preserves the state of the interface area. At the ends of the graph (on the y-axis), it is possible to note

the interface region, i.e., the two liquid films are evidenced around the cavity. These two liquid films have a different effect on the velocity profile in comparison with the gas phase, since the velocity is abruptly reduced at these regions.

Figure 3.9 – Cross-section velocity and liquid fraction profiles for the contact angle of 25°.

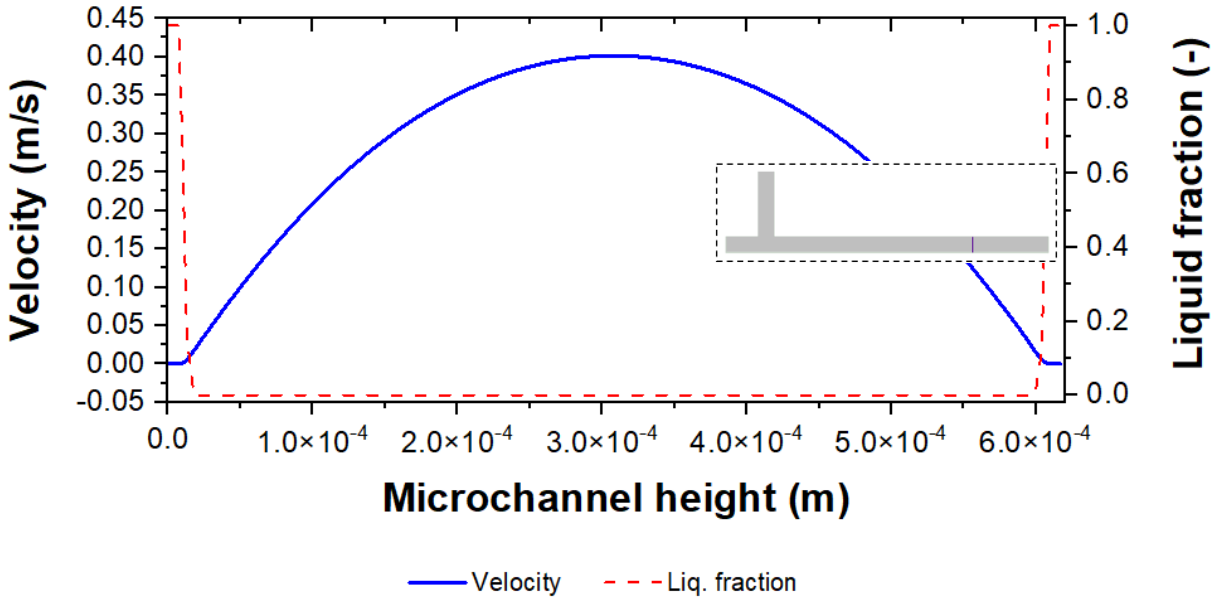


Source: the author (2021).

Axial pressure and liquid fraction profiles along the cavity are shown in Figure 3.10. The overpressure in the cavity due to the Laplace pressure is clearly noticed. As the cavity has a concave shape, the pressure is higher inside this region (Gennes, *et al.*, 2003). Figure 3.11 shows the same behavior, but here the data collected corresponds to the pressure drop per unit length. The pressure jump is related to the cavity passage. Moreover, the pressure drop along the time has another relevant aspect, since it shows the evolution of the numerical simulation regarding the flow development. Indeed, the passage of the second cavity at the region used to extract the pressure drop does not produce significant differences, showing that the results are representative.

Figure 3.10 – Axial pressure and liquid fraction profiles for the contact angle of 25°.

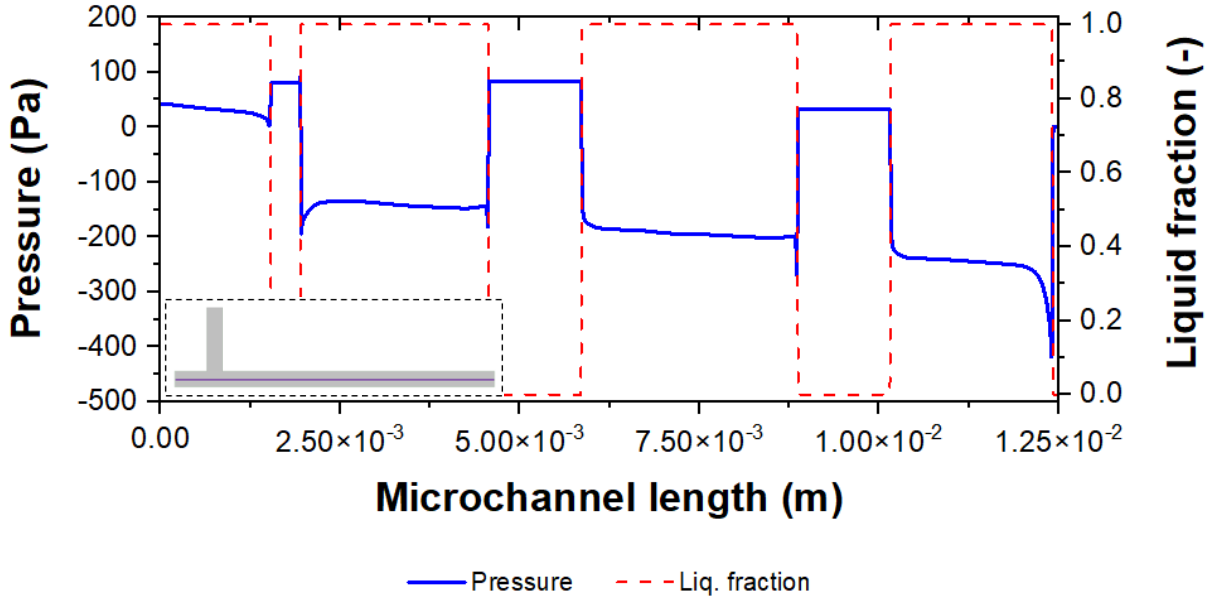


Source: the author (2021).

Figure 3.11 – Transient pressure drop profile for the contact angle of 25°.

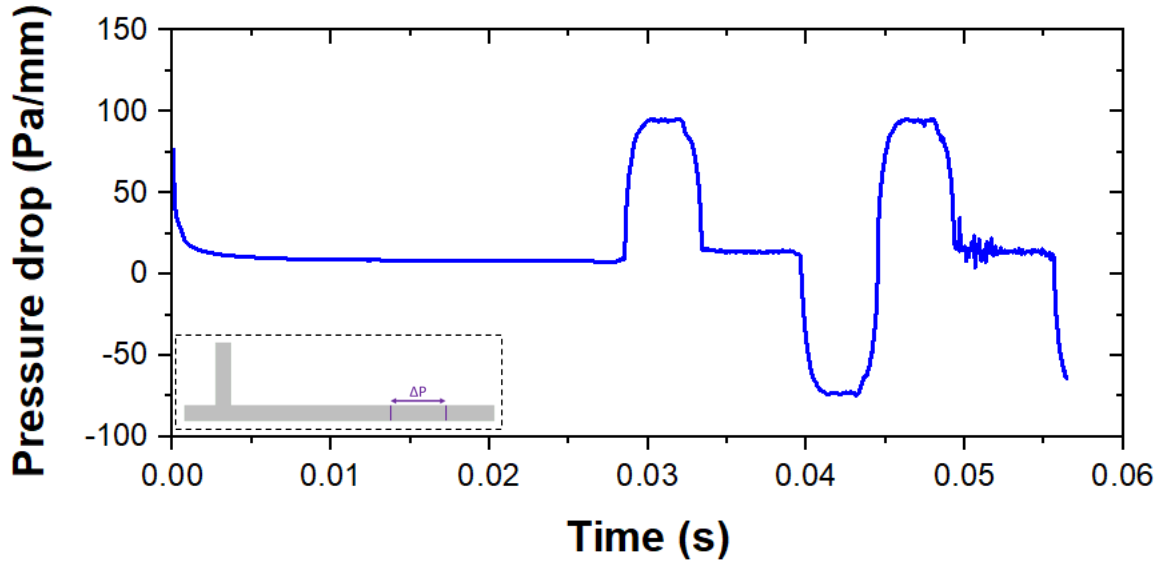


Source: the author (2021).

The quantitative results extracted in the well-developed region of the microchannel are shown in Table 3.1. The pressure was analyzed in two different ways: i) taking into consideration the flow and ii) considering an equilibrium between the two phases. The first one is related to the pressure drop in the microchannel due to the presence of the cavity (taking only one cavity as reference). The correlation proposed for the cavity pressure drop by the experimental study used as the basis for

this work (Choi, *et al*., 2011) resulted in a value of $38.3\ Pa$. Therefore, the numerical result deviated by $7.68\ \%$ from the reference. Another correlation was used to compare the cavity pressure drop, taking into account the analytical pressure drop for a circular duct (Warnier, *et al*., 2010). The value obtained in this case was $38.9\ Pa$, resulting in a variation of $5.91\ \%$ to the numerical result.

The second pressure analysis mentioned is related to the Laplace pressure, i.e., the equilibrium overpressure between the two phases at the interface. An expression accounting for the cavity in in micro-flow was used in this context (Gennes, *et al*., 2003). Interestingly, the numerical model presented a deviation as low as $1.35\ \%$ regarding the calculated value ($225\ Pa$).

In addition, the cavity length obtained experimentally in the work taken as reference for this study (Choi, *et al*., 2011) was $1.45 \cdot 10^{-3}\ \mathrm{m}$, this value was determined by pixel-metering analysis using an image processing software (ImageJ®). The numerical result deviated $7.58\ \%$ from the reference. Lastly, an experimental correlation was used to estimate the liquid film thickness (Han, *et al*., 2010). The value obtained was $9.26 \cdot 10^{-6}\ \mathrm{m}$, resulting in a variation of $18.7\ \%$ relative to numerical result.

Table 3.1 – Information extracted for the contact angle of 25°.

| | |
|---|---|
| Mean cavity pressure drop | $\boldsymbol{41.2\ Pa}$ |
| Laplace pressure | $222\ Pa$ |
| Film thickness | $1.10 \cdot 10^{-5}\ m$ |
| Cavity length | $1.34 \cdot 10^{-3}\ m$ |
| Distance between cavities | $2.93 \cdot 10^{-3}\ m$ |

Source: the author (2021).

*3.3.2.2 Contact angle of 50°*

The importance of wettability on gas-liquid micro-flow is well-known. The contact angle in a tri-phase region (liquid and gas fluids and solid wall) can control the adhesion on the wall and how the cavities will behave (Rosengarten, *et al*., 2006). In addition, experimental work demonstrated the influence of wettability on the flow formation, and the flow pattern can be modified from stratified to bubble only changing

this parameter (Choi, *et al*., 2011). This opens a range of possibilities for investigation and this work focus on analyzing how the flow transition occurs, detailing quantitatively and qualitatively relevant aspects related to the flow pattern.

This section will explore the results obtained for a hydrophilic case, but with a higher contact angle than the previous one. This simulation was performed with a contact angle of 50°, while the previous case considered a contact angle of 25°, i.e., the wettability was reduced leading to lower adhesion of the liquid on the wall (Gennes, *et al*., 2003). However, it is important to mention that this condition still produce cavities, like the previous one, and follow the squeezing mechanism detailed before.

Figure 3.12 shows the squeezing process obtained from the case with contact angle of 50° (along with the velocity vectors). It is evident the interaction between the liquid and the wall even with an increase in the contact angle. The liquid tends to rise in the secondary channel before the cavity separation. The process of cavity growing is the same obtained from the case with contact angle of 25°, i.e., the area for the gas flow is reduced and a process of interface deformation starts. At this moment, the gas phase is not allowed to flow into the main channel anymore and the pressure-velocity field is reorganized. Note that the liquid in the secondary channel starts to be pushed to the main channel.

However, it is possible to note a difference from the previous case with a contact angle of 25°. Now the region that is pushed down contains the portion close to the wall, indicating that the viscous forces are higher than the adhesive forces on the wall. In other words, the wettability effect in this condition is not sufficient to keep the liquid adhered to the solid. This behavior is attributed to the high surface tension and the tendency of getting a round interface. At the end of the process, the wetted area in the secondary channel and the tendency to form a round interface makes the interface to touch the downstream corner of the T-junction, creating a new cavity. Note that the cavity has more difficulty to be generated than the previous case with a contact angle of 25° and it takes more physical time between the beginning of the interface deformation and the moment of cavity generation due to the smaller wetted area on the secondary channel.

A recent work has shown the influence of the contact angle on the flow pattern (Arias, *et al*., 2018). The numerical results indicated a relevant deformation of the interface as the contact angle is increased; higher values of contact angle can lead to a scenario of absence of liquid film, characterizing a flow pattern denominated as non-

lubricated elongated bubble. As previously discussed in the case with a contact angle of 25°, the liquid film around the cavity has to be well-captured when we deal with intermittent micro-flow, but some characteristics could change this requirement and wettability is one of them.

Figure 3.12 – Transient behavior of the cavity formation at the T-junction with a contact angle of 50º (gas in blue and liquid in red).

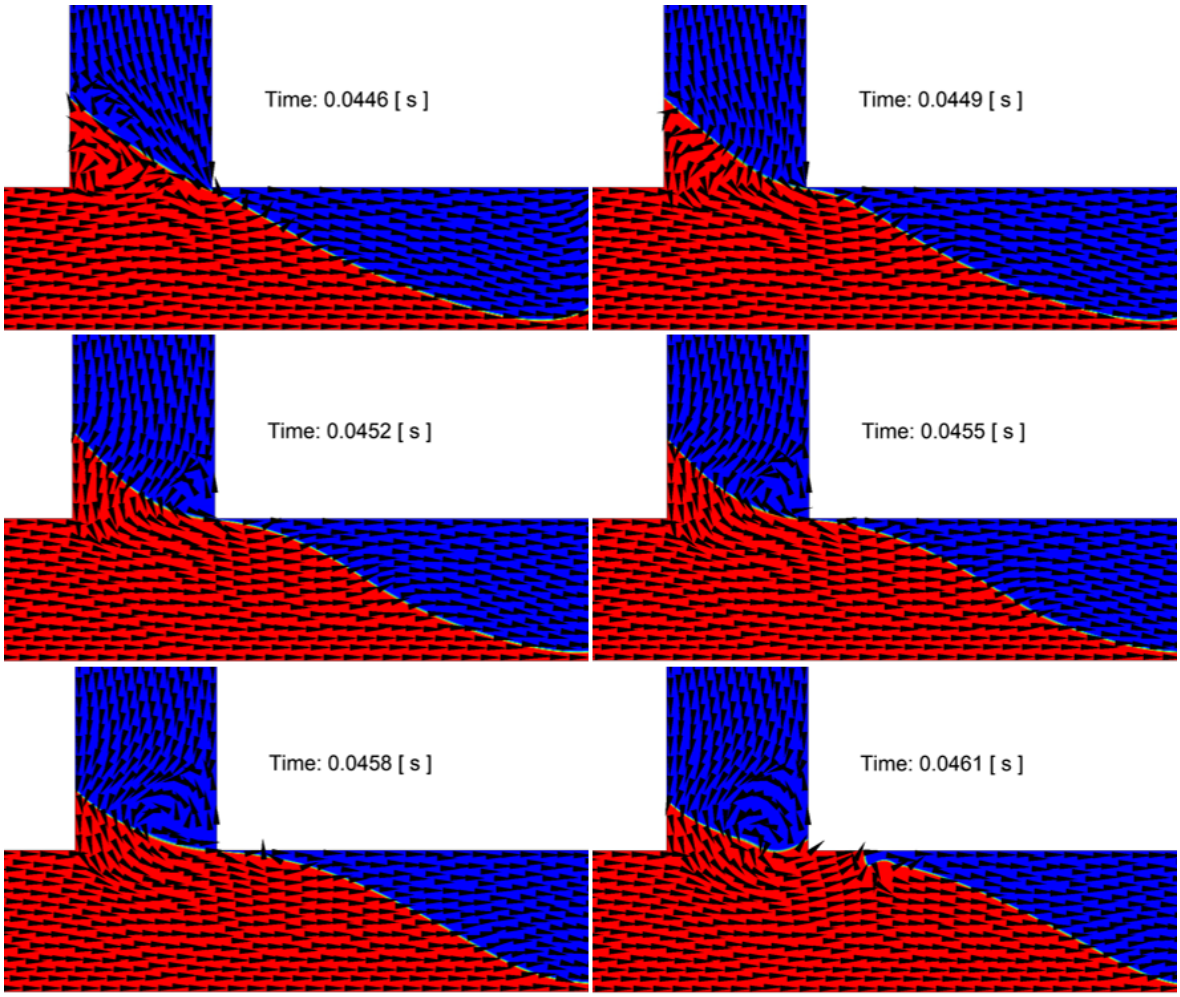


Source: the author (2021).

Figure 3.13 shows the well-developed cavity obtained from the case with contact angle of 50° (along with the velocity vectors). The liquid film (Figure 3.13-c) was captured with a resolution of 5 mesh elements and it developed only in the lower region close to the wall. The interface only touches the upper wall due to the fact that the corner of the T-junction is located on the same wall. It indicates that the viscous forces are higher than the adhesive forces on the wall, and the interface is pushed over

the main channel with absence of a liquid film. On the lower wall, the liquid film is well-comported and is formed as long the cavity is inside the main channel.

Figure 3.13 – Cavity well-developed for the contact angle of 50º (gas in blue and liquid in red): (a) lab reference frame, (b) cavity reference frame and (c) liquid film.

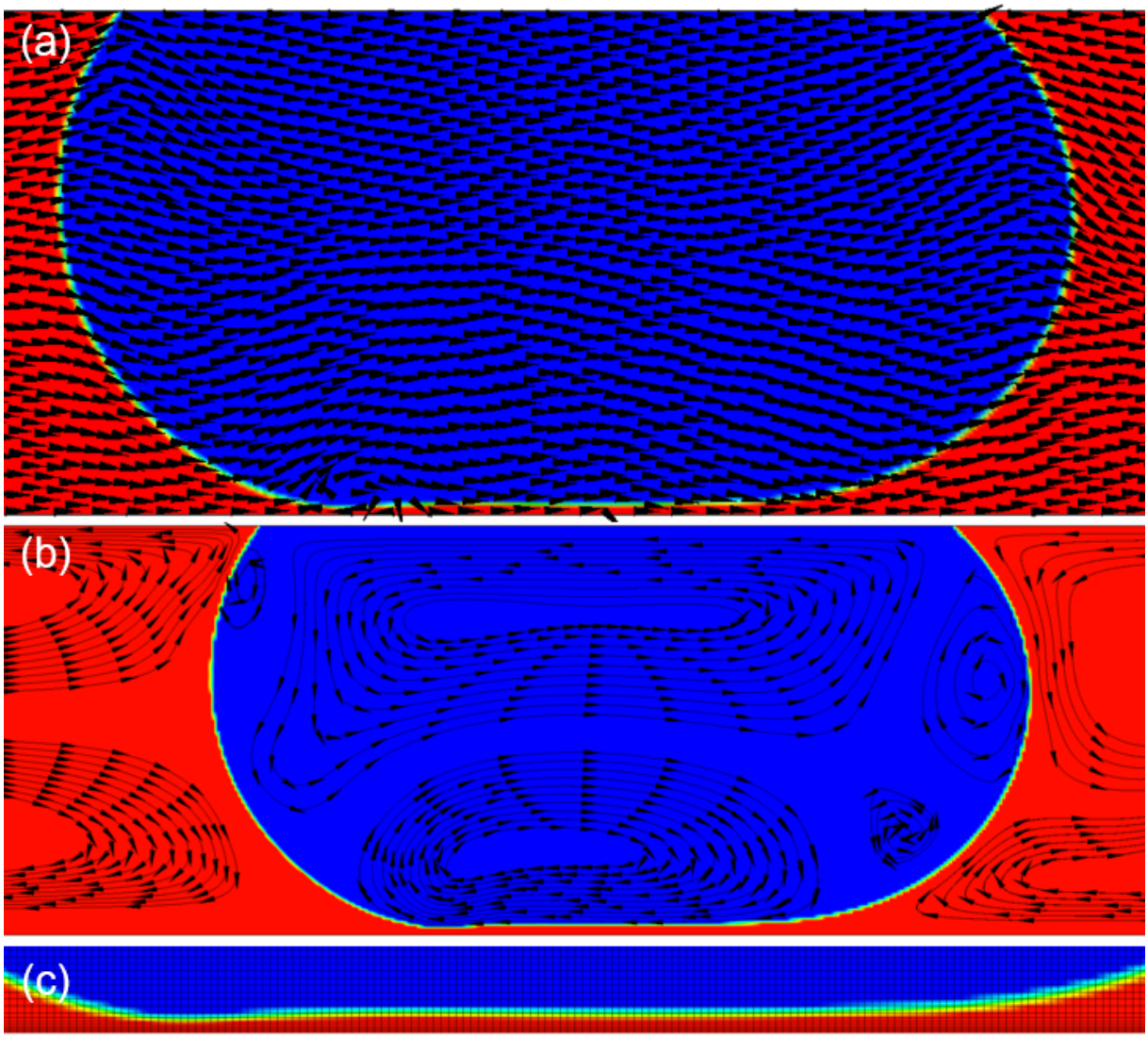


Source: the author (2021).

The velocity vectors on Figure 3.13-a show the presence of parasite currents at the interface region since this pattern has a normal interface parallel to the main flow. The velocity field demonstrated to be well-behaved and aligned with the direction of the main flow. Again, the Taylor recirculation still occurs inside the cavity and in the liquid slug (Figure 3.13-b), resulting in an intensification of heat and mass transfer rates when present. This recirculation is clearly noticed when working with the bubble

reference frame. However, the observation reported herein indicates that a better performance would be obtained for the case of a contact angle of 25° when compared to 50° in terms of intensification of transfer rates. All these features will be explored in a future work.

Figure 3.14 corresponds to the cross-section velocity profile in a cavity (located at the half of the cavity length). The liquid fraction profile was also plotted to better visualize the region of the interface between liquid and the gas phase. The behavior for the cross-section velocity is the same obtained in the previous case with a contact angle of 25°, following a parabolic profile with the highest velocity at the center of the microchannel. At the left side of the graph (in the y-axis), it is possible to note the interface region, i.e., it is demonstrated that the liquid film was only formed in the lower region. Moreover, the liquid film has the same behavior presented on the case with a contact angle of 25°. The velocity is abruptly reduced at this region.

Figure 3.14 – Cross-section velocity and liquid fraction profiles for the contact angle of 50º.

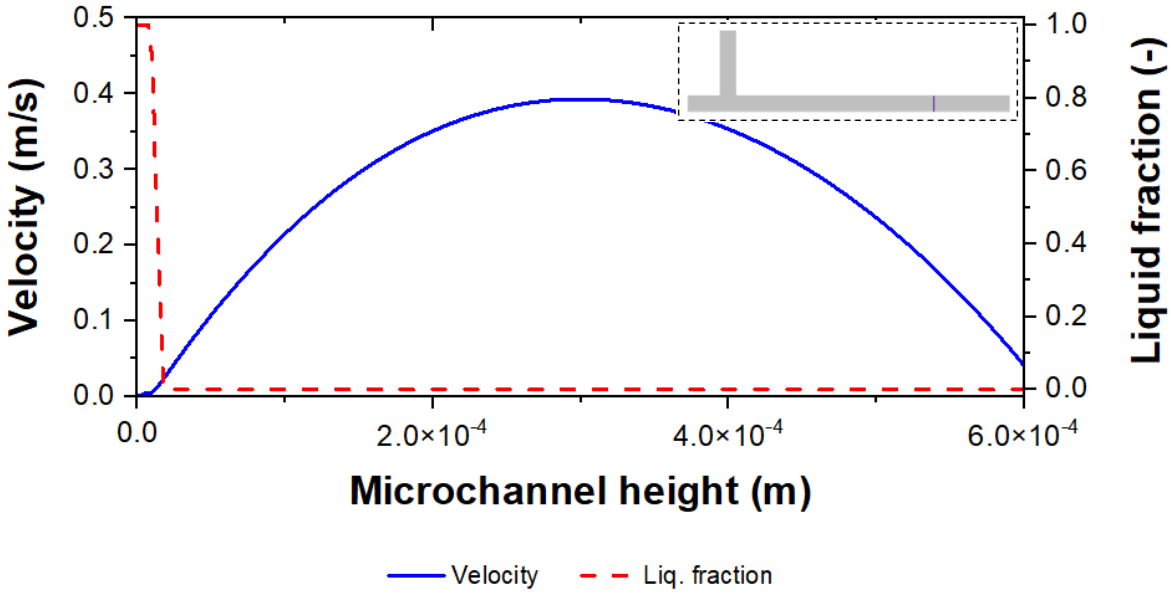


Source: the author (2021).

Regarding the axial profiles (extracted at the center of the microchannel), in Figure 3.15 it is possible to verify the pressure and the liquid fraction over the main channel. The behavior was similar to that obtained from the case with a contact angle

of 25°. As the cavity has a concave shape, the pressure is higher inside the cavity (overpressure), a phenomenon called Laplace pressure (Gennes, *et al*., 2003).

Figure 3.15 – Axial pressure and liquid fraction profiles for the contact angle of 50º.

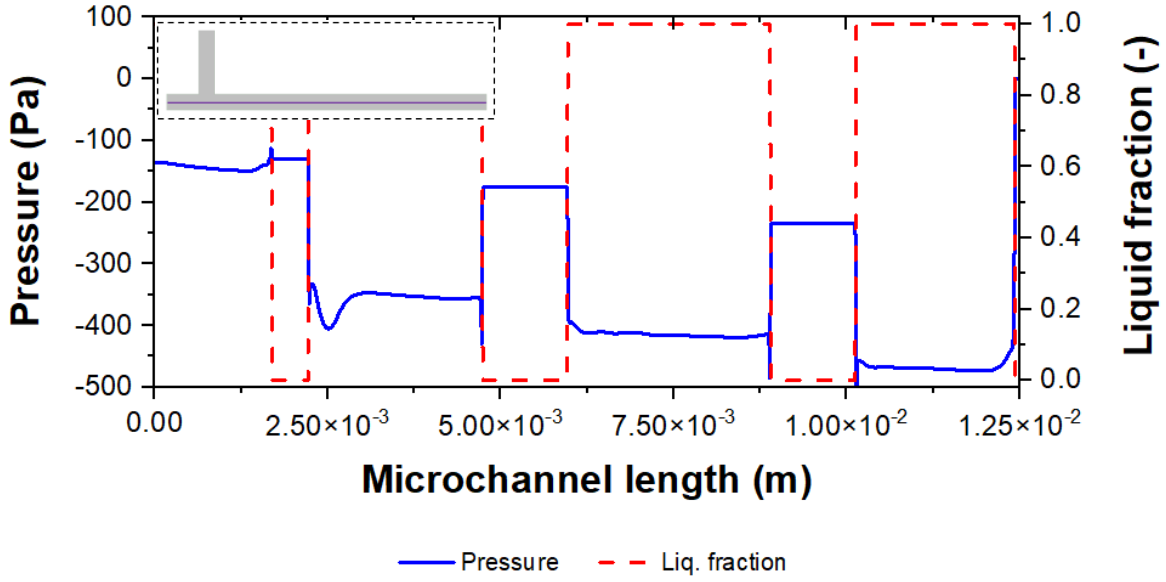


Source: the author (2021).

Figure 3.16 shows the pressure drop per unit length as function of time. The pressure jump is related to the cavity passage. As in the case with a contact angle of 25°, here the pressure drop was used to verify the performance of the numerical simulation when the well-developed flow is obtained. Indeed, the passage of a second cavity in the region used to extract the pressure drop demonstrated that we have a periodical oscillation, showing that the results are quantitatively significant.

Figure 3.16 – Transient pressure drop profile for the contact angle of 50º.

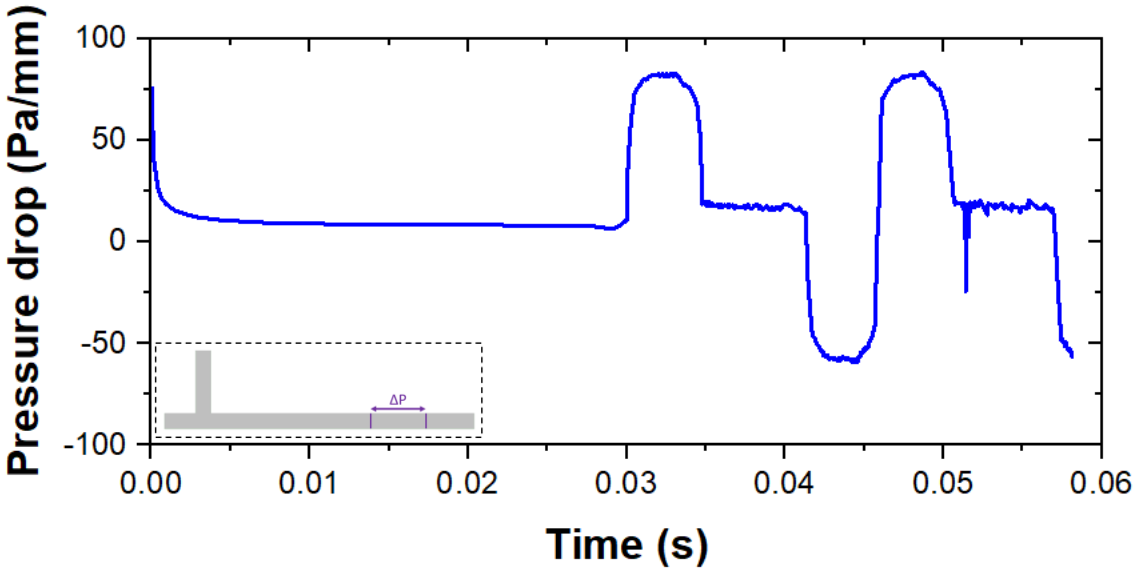


Source: the author (2021).

The quantitative results for the case with a contact angle of 50° are shown in Table 3.2. They were extracted at the well-developed region of microchannel. All the comparisons will be made based on the results obtained from the case with a contact angle of 25°, also resulting in cavities. The cavity without complete lubrification presented an increase on the pressure drop of 23.5 % and a reduction of 17.1 % on the cavity overpressure (Laplace pressure) relative to the case with a contact angle of 25°. These differences are strongly related to the absence of a liquid film at the upper region, i.e., they are related to the reduction of the interfacial area between the two-phases and the wall.

To explain these differences on the pressure we have to mention the capillary force, a well-known capacity of a fluid to rise on a capillary if the conditions are propitious (Gennes, *et al*., 2003). The increase of the cavity pressure drop can be attributed to the energy spent to move the downstream cavity interface over the microchannel. This pattern reduces the action of the capillary force. On the other hand, the absence of a liquid film at the upper region makes the liquid phase to not encompass the cavity and, as a consequence, the interfacial area is reduced, leading to a reduction of the cavity overpressure, since the overpressure is a result of the interaction between the two fluids that form the interface.

Regarding the void fraction and the cavity generation frequency, we do not see many differences from the case with a contact angle of 25º. These two quantities

remained with approximate values, and the cavity length and the distance between the cavities decreased $2.24\ \%$ and $1.01\ \%$, respectively (both values relative to the case with a contact angle of 25º). Lastly, as the case with a contact angle of 50º shows a liquid film only at the lower region, the film thickness increased $16.6\ \%$ relative to the case with a contact angle of 25º, where a liquid film was obtained at the lower and upper regions of the cavity.

Table 3.2 – Information extracted for the contact angle of 50º.

| | |
|---|---|
| Mean cavity pressure drop | $\boldsymbol{50.9\ Pa}$ |
| Laplace pressure | $184\ Pa$ |
| Film thickness | $1.28 \cdot 10^{-5}\ m$ |
| Cavity length | $1.31 \cdot 10^{-3}\ m$ |
| Distance between cavities | $2.90 \cdot 10^{-3}\ m$ |

Source: the author (2021).

*3.3.2.3 Contact angle of 75º*

Up to this point we have observed essentially the formation of cavities with different characteristics in the cases with a contact angle of 25º and 50º. But it is known that the changing the wettability condition can induce a significant change in the flow morphology, resulting even in a stratified pattern. Numerical analysis (Padoin, *et al*., 2016), as well as experimental investigation (Choi, *et al*., 2011), agree with this behavior. For this reason, we have conducted another case with a higher contact angle (reducing the wettability) to evaluate the flow transition.

Figure 3.17 shows the well-developed region obtained from the case with a contact angle of 75º (along with the velocity vectors). The flow pattern is different from the previous cases with a contact angle of 25º and 50º, and a stratified flow pattern was developed. The interface never touches the upper wall on the corner of the T-junction and a cavity can never be formed for this condition. We do not observe the rise of liquid in the secondary channel due to the low wall adherence, causing a serious of modification on the flow characteristics and the squeezing process does not occur in this situation.

Figure 3.17 – Well-developed region for the contact angle of 75º (gas in blue and liquid in red).

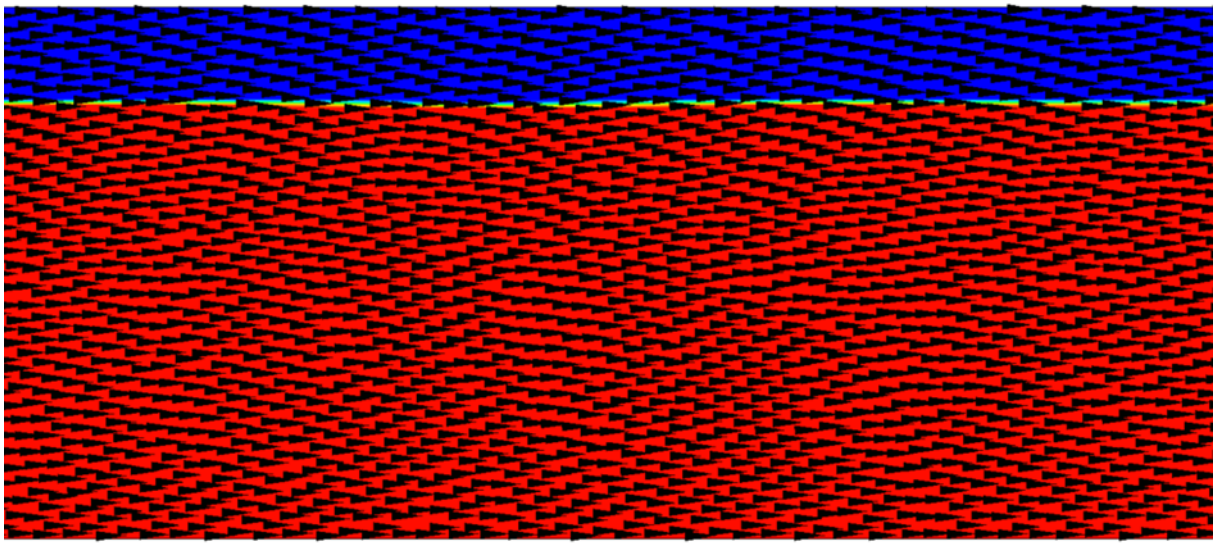

Source: the author (2021).

Even in the case with a contact angle of 50º we have observed that the viscous forces are higher than the adhesive forces on the wall, but this case with a contact angle of 75º increased the ratio between viscous and adhesive forces, resulting in a complete disruption on the flow pattern. The velocity vectors do not show the presence of parasite currents at the interface because this pattern does not have a normal interface parallel to the main flow. The stratified pattern has a lower interfacial area than the previous cases generating intermittent flow. This condition is particularly detrimental in the cases where heat and mass transfer are involved, since the intensification effect on the transfer rates tends to be less pronounced. In fact, it depends not only on the interfacial area available for exchanges but also on the velocity field (presence of recirculation, for instance). Therefore, this is a highly non-linear problem that will be solved in a future study to precisely demonstrate the effect of the flow pattern induced by the variables evaluated herein on different transport phenomena occurring in micro-flow. Finally, it should be noted that the velocity field demonstrated to be well-behaved and aligned with the direction of the main flow for the contact angle of 75º (considering the lab reference frame).

Figure 3.18 corresponds to the cross-section velocity profile. The liquid fraction was also plotted to better visualize the region of interface between the liquid and the gas phase. The velocity behavior is different from that obtained in the cases with

contact angles of 25º and 50º. The case with a contact angle of 75º presents two layers well-comported. The layer located in the lower region is the liquid due to the position of the inlets. On the other hand, the gas is confined in the upper layer. The gas velocity is increased to ensure mass conservation (liquid occupies a larger part of the microchannel). At the right side of the graph, it is possible to note the exact interface region, since this region determines the point of change for the velocity profile.

Figure 3.18 – Cross-section velocity and liquid fraction profiles for the contact angle of 75º.

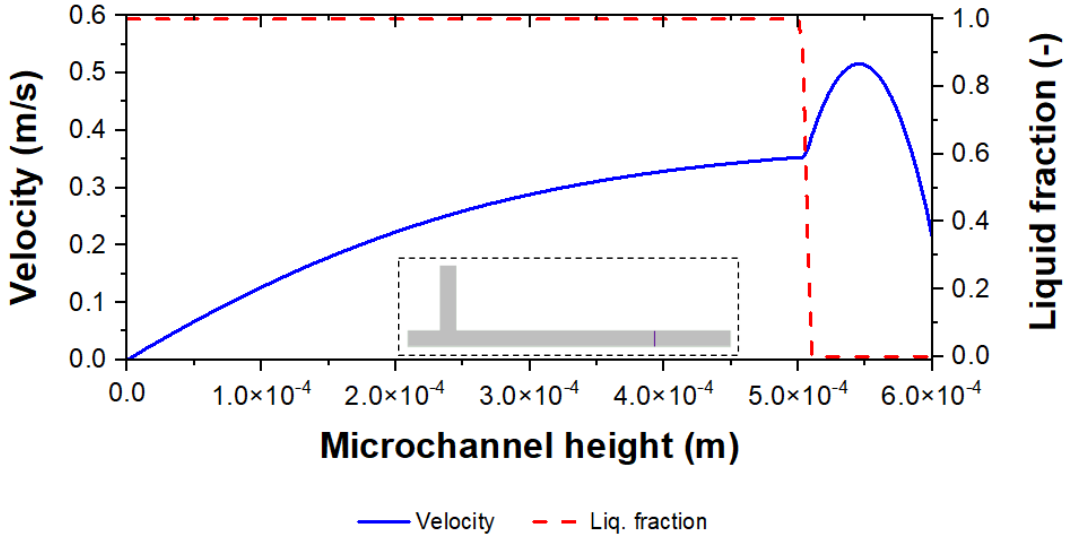


Source: the author (2021).

The pressure drop was analyzed to ensure that we have achieved a well-developed flow as in the previous cases. Figure 3.19 shows the pressure drop per unit length as a function of time. Different from the previous cases, there is not cavity formation in this case, and it brings us to a completely different behavior for the pressure drop profile. After an initial transient instability, we achieve a constant value for the pressure drop (which does not suffer significant changes over time), showing that the results are quantitatively significant.

Figure 3.19 – Transient pressure drop profile for the contact angle of 75º.

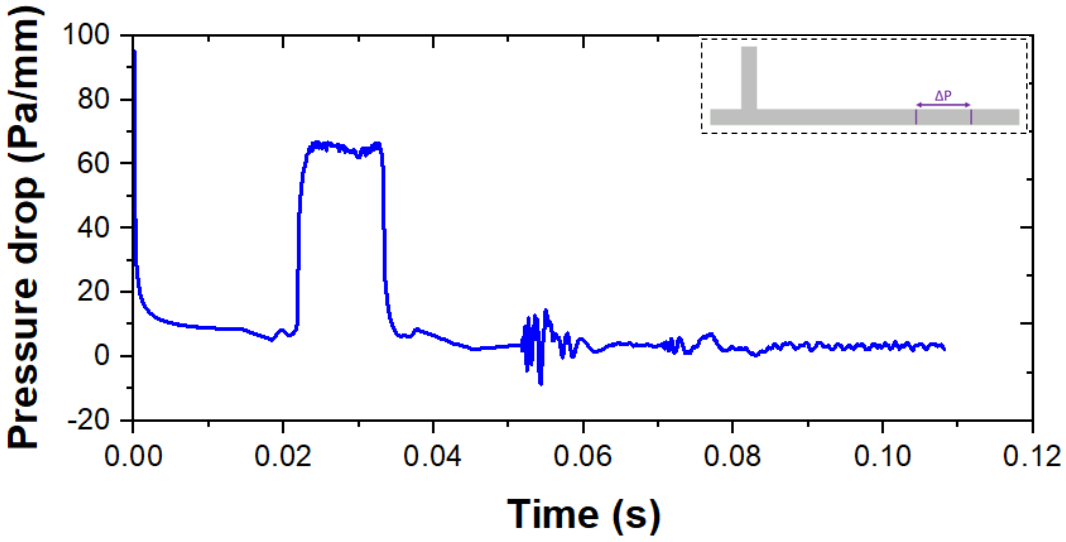


Source: the author (2021).

The quantitative results for the case with a contact angle of 75º are shown in Table 3.3. They were extracted at the well-developed region of microchannel. The pressure drop reduced $80\%$ relative to the case with a contact angle of 50º, resulting in a partially non-lubricated cavity. The difference in the pressure drop between stratified and intermittent flow is known (Yin, *et al*., 2019). When we have a two-layer flow (or stratified), the interface friction reduces, and each fluid can flow without competing with another. Consequently, the pressure drop is reduced. Lastly, it should be mentioned that the gas layer occupies only $19\ \%$ of the main channel.

Table 3.3 – Information extracted for the contact angle of 75º.

| | |
|---|---|
| Mean channel pressure drop | $\boldsymbol{3.3\ Pa/mm}$ |
| Gas layer thickness | $1.17 \cdot 10^{-4}\ m$ |

Source: the author (2021).

### 3.3.3 Contribution of the momentum equation source term on the flow pattern

#### *3.3.3.1 T-junction region*

The mixing region is the most important part to the flow pattern development in micro-flow, and some variations of the junction geometry can change the cavity

behavior (Lim, *et al*., 2019). Also, variations on wettability impact on different levels of liquid rise in the secondary channel. Consequently, these are key factors for a transition from an intermittent to a stratified flow pattern. Complementing the previous discussion focused on the well-developed flow region and cavity formation mechanism, this section will explore the T-junction region.

Figure 3.20 shows the behavior of the interface at the T-junction in the moment before the cavity formation (for the cases that formed a cavity since the stratified flow has permanent aspect) for three contact angles analyzed, 25º, 50º and 75º. Each line in the image reflects the height that the liquid reaches. It is possible to see a reduction on the liquid rise as the contact angle is increased, indicating a reduction of the adhesive forces on the wall. The greater the height, the bigger will be the interface curvature at the T-junction region, indicating a relevant role of surface tension. Consequently, cavity formation will be facilitated in this scenario.

Figure 3.20 – Behavior of the interface at the T-junction for different contact angles.

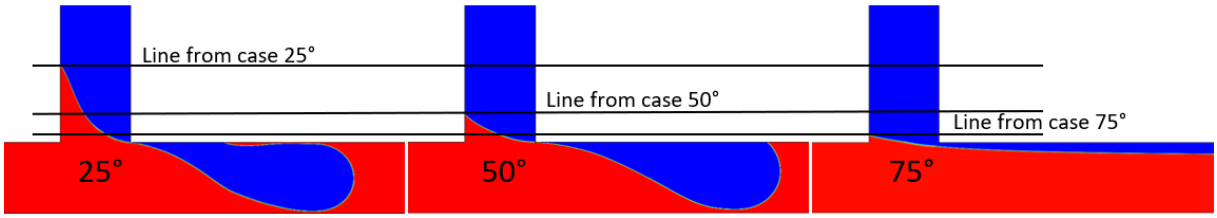


Source: the author (2021).

The quantification of the liquid height in the secondary channel as a function of the contact angle is shown in Figure 3.21. The liquid height is expressed as a fraction of the microchannel diameter to better analyze the results. Clearly, the liquid height follows an exponential function, tending to zero when the contact angle reaches 90º. The cases with a contact angle of 25º and 50º resulted in a height of $1.09$ and $0.35$ times the diameter, respectively. These two cases were able to generate cavities. However, the case with a contact angle of 75º resulted in a height of $0.10$ times the diameter and a stratified pattern was formed, indicating that the values below $0.35$ will not produce an intermittent pattern.

Figure 3.21 – Liquid height in the secondary channel for different contact angles.

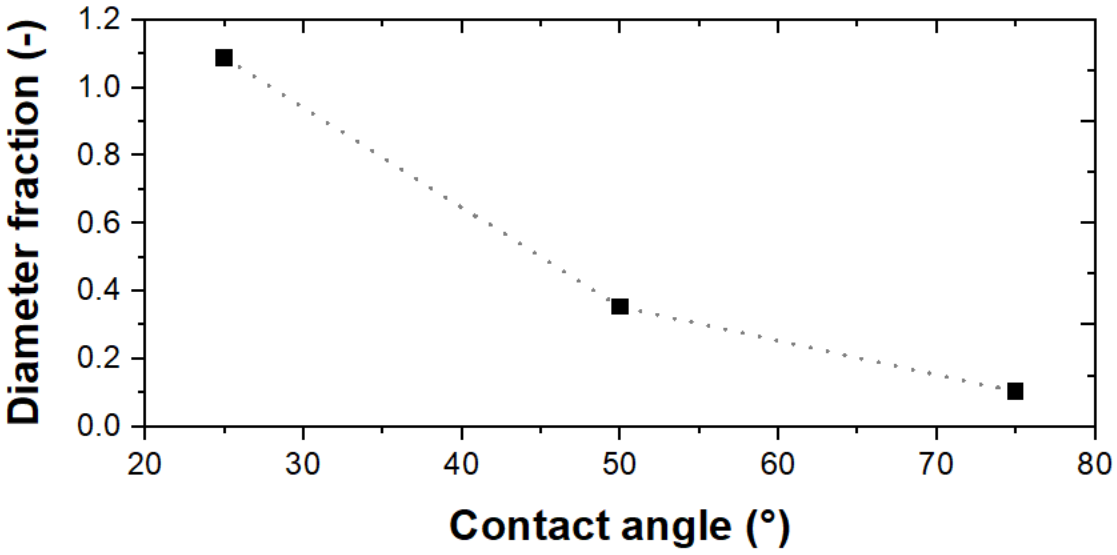


Source: the author (2021).

It is possible to correlate the previous observations with the source term of the momentum equation. This term appears due to the multiphase VOF model and accounts the interfacial interaction between fluids (Fluent, 2019), according to Eq. 3.22.

$$interfacial\ source\ term = \sigma\kappa \frac{\rho \nabla \alpha_g}{\frac{1}{2}(\rho_l + \rho_g)} \tag{3.22}$$

In the three cases analyzed, the surface tension ($\sigma$) was kept constant. But when the contact angle is varied, the curvature ($\kappa$) on the wall will change. Basically, the curvature on the wall decreased with the increase of the contact angle (until 90º), because adhesive forces decrease and the liquid is less “wet”. Moreover, the unit normal vector of the interface on the wall starts to be influenced only by the tangential term, justifying the pushing of the interface over the wall in the case with a contact angle of 50º. As a result, the greater the contact angle, the lower will be the curvature and the source term will be reduced. Consequently, a stratified pattern will be formed. It is expected that the lower the source term, the more propitious will be to generate a stratified pattern.

*3.3.3.2 Case with reduced surface tension*

As previous showed, when we vary wettability, through the contact angle, we are reducing the surface curvature on the wall and the magnitude of the source term of the momentum equation will be also reduced. But we can produce the same behavior changing the surface tension. The lower the surface tension, the smaller will be the source term.

Surface active agents are usually added to increase stability of the cavities or bubbles in multiphase flow. The so-called surfactants can significantly reduce the surface tension between two fluids (Roumpea, *et al*., 2019). In order to demonstrate the flow pattern change discussed in the previous results, a case with a reduced surface tension (half of the value used on previous simulations) was carried with a contact angle of 50º.

Figure 3.22 shows the well-developed and T-junction region obtained from the case with a contact angle of 50º and reduced surface tension (along with the velocity vectors). The flow pattern is different from the case with a contact angle of 50º and with the standard surface tension. A stratified flow pattern was developed, demonstrating the impact of the source term. It was observed that the case with higher surface tension (standard value) was already close to the limit between stratified and intermittent flow, and a reduction in the source term (using a lower surface tension) was able to cross the limit between both regimes, generating a stratified pattern due to the contribution of the source term (previously discussed). As in the previous cases, the velocity vectors do not show the presence of parasite currents and the velocity field demonstrated to be well-behaved and align with the direction of the main flow. The T-junction region shows the same liquid height in the secondary channel obtained in the case with a higher surface tension with the same contact angle. But due to reduced surface tension used on this case the interface is more malleable, inducing to higher curvature at the T-junction region, leading to the modification of the flow pattern.

Figure 3.22 – Interface for the contact angle of 50º and reduced surface tension (gas in blue and liquid in red): (a) well-developed region, (b) T-junction region.

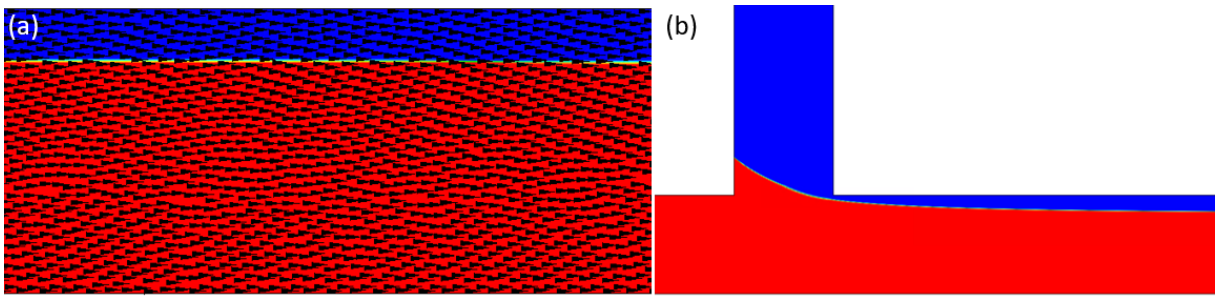


Source: the author (2021).

Figure 3.23 corresponds to the cross-section velocity profile. The liquid fraction profile is also plotted to better visualize the region of interface between the liquid and the gas phase. The velocity behavior is the same from that obtained in the case with a contact angle of 75º using a higher surface tension (standard value). It is possible to visualize two layers well-comported. The gas is confined in the upper layer and has an increased velocity to ensure mass conservation (since liquid occupies a larger part of the microchannel).

The pressure drop was analyzed to ensure that we have achieved a well-developed flow as in the previous cases. Figure 3.24 shows the pressure drop per unit length as a function of time. Again, we see the same behavior obtained in the case with a contact angle of 75º. There is no formation of cavities and after the initial instability we achieve a constant value for the pressure drop (which does not suffer significant changes over time). This observation justifies the quantitative relevance of the results obtained.

Figure 3.23 – Cross-section velocity and liquid fraction profiles for the contact angle of 50º and reduced surface tension.

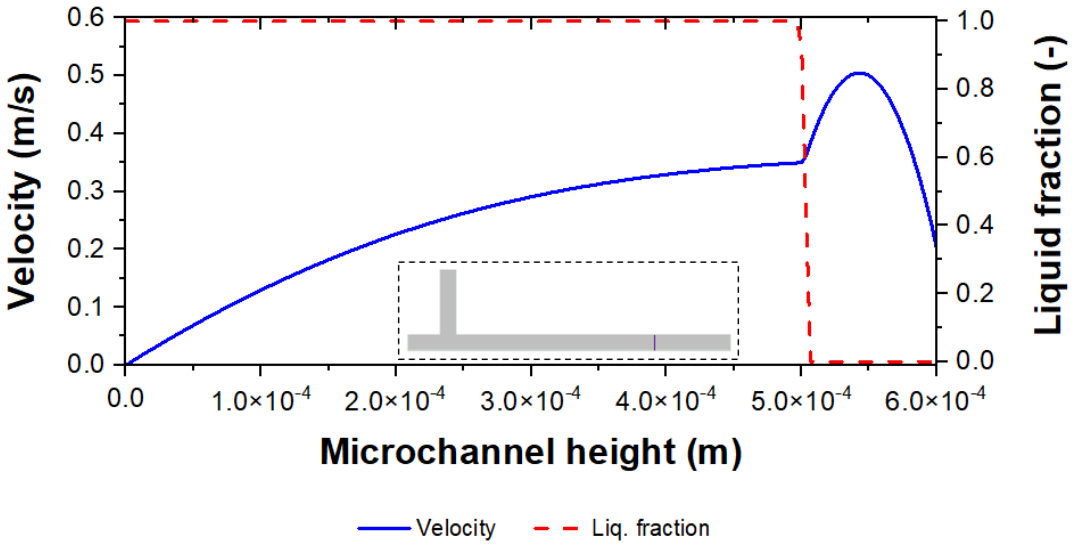


Source: the author (2021).

Figure 3.24 – Transient pressure drop profile for the contact angle of 50º and reduced surface tension.

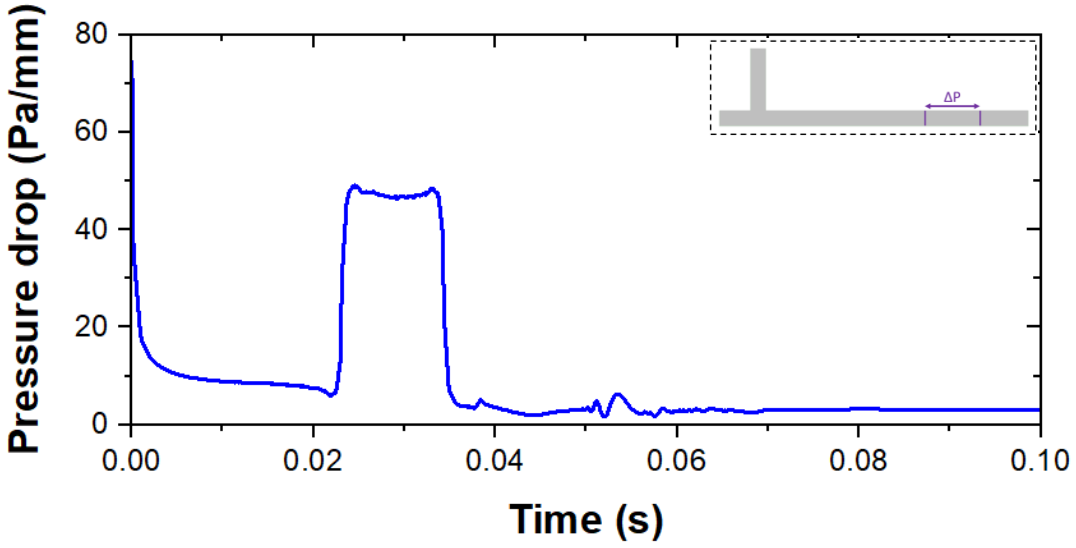


Source: the author (2021).

The quantitative results for the case with a contact angle of 50º and reduced surface tension are shown in Table 3.4. They were extracted in the well-developed region of microchannel. The pressure drop reduced 6.6% and the gas layer increased 2.56% relative to the case with a contact angle of 75º and a higher surface tension (this case was chosen for comparison since the same flow pattern was obtained).

The increase of the gas layer thickness can be attributed to the lower surface tension. As the surface is more malleable, the gas flow pushes the interface down on the T-junction, creating an equilibrium different from the scenario observed with a higher surface tension, and increasing the gas layer thickness. Consequently, the gas occupies more space in the microchannel, and to ensure mass conservation the velocity of this phase is reduced. The pressure drop is closely related to the velocity of the phase. As velocity is reduced, the pressure drop is also reduced.

Table 3.4 – Information extracted for the contact angle of 50º and reduced surface tension.

| | |
|---|---|
| Mean pressure drop per unit length | $\boldsymbol{3.08\ Pa/mm}$ |
| Gas thickness | $1.20 \cdot 10^{-4}\ m$ |

Source: the author (2021).

## 3.4 CONCLUSIONS

Over the last decade, an effort has been noted to understand and propose mechanisms for micro-flow. Commonly, these devices are used for process intensification due to the higher degree of system control, a key factor when dealing with multiphase flow patterns.

This study contemplates a computational multiphase analysis with different wettability effects on the wall, considering a range for contact angle (25º to 75º), illustrates the phenomena that occur in each operation condition and explains how a transition between intermittent and stratified pattern can be produced.

Before starting the numerical analysis, it was needed to build a computational grid for the domain and some concerns were discussed regarding the grid arrangement. It is necessary to align the grid with the flow streamlines and take care of the maximum aspect ratio of the cells to avoid unphysical results like numerical diffusion. It is recommended a maximum value of 5 for the aspect ratio, otherwise it will produce cells with a high distortion for the multiphase analysis.

To ensure reliability of the results, the base case was confronted with experiments and correlations available in the literature. The case with a contact angle of 25º forming an intermittent pattern with a liquid film around the entire cavity was

used to validate the simulations and the results showed good agreement for the pressure drop per cavity, Laplace pressure, cavity length and film thickness.

The variation of wettability through the contact angle was systematically explored. The main observation was the transition from intermittent to stratified pattern as the wettability is reduced, i.e., increasing the contact angle. Over the transition process, it was noted that in some conditions the liquid film around the entire cavity is not formed, allowing the flow to push the interface that touches the wall over the microdevice length, and this behavior could be attributed to the reduction of adhesive forces on the wall relative to the viscous forces. Squeezing mechanism to generate cavities was observed, but with a variation on the velocity field as the contact angle was increased.

An analysis about the source term of the momentum equation was useful to understand how the modification on the flow pattern occurred when varying the wettability and how the same effects could be extended to other properties. The lower the source term, the smaller will be the interfacial effects and a stratified pattern is expected. The same behavior was observed when varying the surface tension. A reduced surface tension for the same set of operation conditions produced a stratified pattern. On the other hand, when a higher surface tension is used (standard value), an intermittent pattern was achieved.

# 4 CONCLUDING REMARKS AND RECOMMENDATIONS FOR FUTURE WORKS

The author believes that this document can contribute to the development of science, specifically on process intensification in microdevices, in the great field of Engineering.

This work presented a computational fluid dynamics approach for the simulation of gas-liquid micro-flow. The commercial solver ANSYS® CFD (Fluent®), version 19.2, was used to solve a two-dimensions model. The study was divided into two parts. The first part dealt with numerical aspects, looking for the optimum condition to conduct a numerical simulation of gas-liquid micro-flow. The second part is related to the analysis of the fluid flow pattern as a function of the wettability.

Firstly, during the study of the wettability effect on micro-flow, it was noted an undesirable effect on the simulation results. An exceedingly difficult to reproduce a specific scenario was noted and it seemed that each run converged to a different result. This behavior violates the determinist principle of CFD techniques. With this in mind, the author sought for an explanation and the answer relied on non-independent results. In other words, if some change occurred on a numerical or discretization parameter, a different result could be generated. It is important to point out that at this stage the discretization and resolution were similar to that found in the literature and it is attributed to the low Capillarity number, which indicates a higher predominance of the surface tension forces, the requirement of a precise independence study to ensure reproducibility.

Among the contributions of this work, it is possible to highlight a systematic study of the effect of numerical and discretization parameters on the performance of gas-liquid micro-flow simulations. A methodology was created to verify the influence of iteration convergence. Moreover, the dependency of space and time domain were also investigated. It was possible to determine the optimum condition to numerically solve the computational model on a situation where the interface has a major role in the fluid flow.

In addition, another contribution consists of the understanding of the effect of transition between intermittent and stratified pattern due to the wettability. One of the most relevant results was the possibility of not having a liquid film around the cavity. This is ostensibly described in the literature as something fundamental on intermittent flow.

As any scientific study, one conclusion opens the way for several questions with the intention to expand the scientific knowledge. This work provided the following ideas regarding future work for multiphase simulation studies:

- Regarding the numerical model, verify if gravity has some impact on the microflow. Besides to evaluate analysis with higher relaxation factor, adaptive mesh and multi-VOF model.
- Implement additional source term to reduce the generation of parasite currents and estimate more precisely the surface curvature to be able to calculate the pressure drop at the interface the closest from the analytical result.
- Evaluate different angles between the two channels at the inlet region. In addition, investigate different aspect ratio between these two channels, i.e., varying the diameter of each channel. This will modify completely the interaction between the two phases.
- Evaluate different fluids to vary the Capillarity number and different flow rates to vary the Webber number. This is useful to investigate the fluid flow behavior in terms of dimensionless numbers perspective.
- Insert heat and mass transfer mechanisms in the computational model. It will be necessary to evaluate a complementary study of numerical independence to consider the heat and mass transfer phenomena.
- Evaluate different geometry scales to analyze the transition effects between macro and micro flow scale.

## REFERENCES

**Arias S. and Montlaur A.** Influence of Contact Angle Boundary Condition on CFD Simulation of T-Junction [Journal]. - [s.l.] : Microgravity-Science and Technology, 2018.

**Brennen Christopher E.** Fundamentals of Multiphase Flows [Book]. - [s.l.] : Cambridge University Press, 2005.

**Bretherton F. P.** The motion of long bubbles in tubes [Journal]. - [s.l.] : Journal of Fluid Mechanics, 1961. - Vol. 10.

**Chen Jinfang [*et al*.]** Gas–liquid two-phase flow splitting at microchannel junctions with different branch angles [Journal]. - [s.l.] : Chemical EngineeringScience, 2013. - Vol. 104.

**Chirco L., Da Vià R. and Manservisi S.** VOF evaluation of the surface tension by using variational representation and Galerkin interpolation projection [Journal]. - [s.l.] : Journal of Computational Physics, 2019. - Vol. 395.

**Choi Chiwoong, In Yu Dong and Kim Moohwan** Surface wettability effect on flow pattern and pressure drop in adiabatic [Journal] // Experimental Thermal and Fluid Science. - 2011. - pp. 1086-1096.

**Convery Neil and Gadegaard Nikolaj** 30 years of microfluidics [Journal]. - [s.l.] : Micro and Nano Engineering, 2019. - Vol. 2.

**Faust Jennifer and House James E.** Physical Chemistry of Gas-Liquid Interfaces [Book]. - [s.l.] : Elsevier, 2018.

**Fletcher David F and Haynes Brian S** CFD simulation of Taylor flow: Should the liquid film be captured or not? [Journal]. - [s.l.] : Chemical EngineeringScience, 2016.

**Fletcher David F. [*et al*.]** Modelling of microfluidic devices [Journal]. - [s.l.] : Micro Process Engineering, 2009. - Vol. 1.

**Fluent** Documentation v19 [Book]. - [s.l.] : Ansys Inc., 2019.

**Garstecki Piotr [*et al*.]** Formation of droplets and bubbles in a microfluidic T-junction—scaling and mechanism of break-up [Journal]. - [s.l.] : Lab on a Chip, 2006.

**Gennes Pierre Gilles, Wyart Françoise Brochard and Quéré David** Capillarity and Wetting Phenomna: Drops, Bubbles, Pearls, Waves [Book]. - [s.l.] : Springer, 2003.

**Gnedin Nickolay Y., Semenov Vadim A. and Kravtsov Andrey V.** Enforcing the Courant–Friedrichs–Lewy condition in explicitly conservative local time stepping schemes [Journal]. - [s.l.] : Journal of Computational Physics, 2018. - Vol. 359.

**Gupta R., Fletcher D.F. and Haynes B.S.** Taylor Flow in Microchannels: A Review of Experimental and Computational Work [Journal]. - [s.l.] : Journal of Computational Multiphase Flows, 2010. - Vol. 2.

**Han Youngbae and Shikazono Naoki** The effect of bubble acceleration on the liquid film thickness in micro tubes [Journal]. - [s.l.] : International Journal of Heat and Fluid Flow, 2010. - Vol. 31.

**Harvie D.J.E., Davidson M.R. and Rudman M.** An analysis of parasitic current generation in Volume of Fluid simulations [Journal]. - [s.l.] : Applied Mathematical Modelling, 2005. - Vol. 30.

**Ho Chih-Ming and Tai Yu-Chong** MICRO-ELECTRO-MECHANICAL-SYSTEMS (MEMS) AND FLUID FLOWS [Journal]. - [s.l.] : Annual Review of Fluid Mechanics, 1998. - Vol. 30.

**Kovalchuk Nina M. [*et al*.]** Effect of surfactant on emulsification in microchannels [Journal]. - [s.l.] : Chemical Engineering Science, 2018. - Vol. 176.

**LANEY CULBERT B.** Computational Gasdynamics [Book]. - [s.l.] : Cambridge University Press, 1998.

**Lee Chi Young and Lee Sang Yong** Influence of surface wettability on transition of two-phase flow pattern in round mini-channels [Journal]. - [s.l.] : International Journal of Multiphase Flow, 2008. - Vol. 34.

**Lim An Eng [*et al*.]** Effect of microchannel junction angle on two-phase liquid-gas Taylor flow [Journal]. - [s.l.] : Chemical Engineering Science, 2019. - Vol. 202.

**Malekzadeh Shima and Roohi Ehsan** Investigation of Different Droplet Formation Regimes in a T-junction Microchannel Using the VOF Technique in OpenFOAM [Journal]. - [s.l.] : Microgravity Science and Technology, 2015. - Vol. 27.

**Maliska Clovis R.** Transferência de Calor e Mecânica dos Fluidos Computacionais [Book]. - [s.l.] : LTC, 2004.

**Méndez Norma A. Noguez [*et al*.]** Chapter 22 - Design and development of pharmaceutical microprocesses in the production of nanomedicine [Book]. - [s.l.] : Nanostructures for Oral Medicine, 2017.

**Nazari Mohsen [*et al*.]** Different Stages of Liquid Film Growth in a Microchannel: Two-Phase Lattice Boltzmann Study [Journal]. - [s.l.] : Brazilian Journal of Chemical Engineering, 2018. - Vol. 35.

**Oishi Masamichi [*et al*.]** Investigation of Micro Droplet Formation in a T-Shaped Junction Using Multicolor Confocal Micro PIV [Journal]. - [s.l.] : Micro/Nanoscale Heat Transfer International Conference, 2008.

**Padoin Natan [*et al*.]** Numerical Simulation of Isothermal Gas-Liquid Flow Patterns in Microchannels with Varying Wettability [Journal]. - [s.l.] : Chemical Engineering Research and Design, 2016. - Vol. 109.

**Pan Z., Weibel J.A. and Garimella S.V.** Spurious Current Suppression in VOF-CSF Simulation of Slug Flow through Small Channels [Journal]. - [s.l.] : Numerical Heat Transfer Applications, 2015. - Vol. 67.

**Popinet Stéphane** An accurate adaptive solver for surface-tension-driven interfacial flows [Journal]. - [s.l.] : Journal of Computational Physics, 2009. - Vol. 228.

**Ralston John, Popescu Mihail and Sedev Rossen** Dynamics of Wetting from an Experimental Point of View [Journal]. - [s.l.] : Annual Review of Materials Research, 2008. - Vol. 38.

**Rosengarten G., Harvie D. J. E. and Cooper-White J.** Contact angle effects on microdroplet deformation using CFD [Journal]. - [s.l.] : Applied Mathematical Modelling, 2006. - Vol. 30.

**Roumpea Evangelia [*et al*.]** Experimental studies on droplet formation in a flow-focusing microchannel in the presence of surfactants [Journal]. - [s.l.] : Chemical Engineering Science, 2019. - Vol. 195.

**Song Yuexiao [*et al*.]** Uniform generation of water slugs in air flowing through superhydrophobic microchannels with T-junction [Journal]. - [s.l.] : Chemical Engineering Science, 2019.

**Warnier M. J. F. [*et al*.]** Pressure drop of gas–liquid Taylor flow in round micro-capillaries for low to intermediate Reynolds numbers [Journal]. - [s.l.] : Microfluid Nanofluid, 2010. - Vol. 8.

**Wörner Martin** Numerical modeling of multiphase flows in microfluidics and micro process engineering: a review of methods and applications [Journal]. - [s.l.] : Microfluid Nanofluid, 2012. - Vol. 12.

**Yin Liaofei [*et al*.]** Heat transfer and pressure drop characteristics of water flow boiling in open microchannels [Journal]. - [s.l.] : International Journal of Heat and Mass Transfer, 2019. - Vol. 137.